LABORATORY ANALYSIS OF VORTEX DYNAMICS FOR SHALLOW TIDAL INLETS

A Thesis

by

KERRI ANN WHILDEN

Submitted to the Office of Graduate Studies of
Texas A&M University
in partial fulfillment of the requirements for the degree of

MASTER OF SCIENCE

August 2009

Major Subject: Ocean Engineering

LABORATORY ANALYSIS OF VORTEX DYNAMICS FOR SHALLOW TIDAL INLETS

A Thesis

by

KERRI ANN WHILDEN

Submitted to the Office of Graduate Studies of
Texas A&M University
in partial fulfillment of the requirements for the degree of

MASTER OF SCIENCE

Approved by:

Co-Chairs of Committee,	Scott Socolofsky
	Kuang-An Chang
Committee Members,	Robert Hetland
Head of Department,	David V. Rosowsky

August 2009

Major Subject: Ocean Engineering

ABSTRACT

Laboratory Analysis of Vortex Dynamics

for Shallow Tidal Inlets. (August 2009)

Kerri Ann Whilden, B.S., Lehigh University

Co–Chairs of Advisory Committee: Dr. Scott Socolofsky
Dr. Kuang-An Chang

Estuaries depend on the transport of nutrients and sediments from the open sea to help maintain a prosperous environment. One of the major transport mechanisms is the propagation of large two dimensional vortical structures. At the mouth of an inlet, tidal flow forces the formation of two dimensional vortical structures whose lateral extent is much greater than the water depth. After the starting jet vortex dipole detaches from the inlet, secondary vortices shed due to separation from the inlet boundary and eventually reach the starting-jet dipole. An idealized inlet configuration was utilized for laboratory experiments detailing the formation and propagation of the vortex structures with water depths of 3, 5, and 9 centimeters and flow Froude scaled to inlets along the Texas coast. Using surface particle image velocimetry, the entrainment of the secondary structures into the vortex system are shown as well as variations in characteristics such as trajectory, size, vorticity, and circulation for the vortices as they move downstream.

To the loved ones who have encouraged me along the way.

ACKNOWLEDGMENTS

The research presented in this thesis was funded by an institutional grant to Texas A&M University by the National Sea Grant Office, National Oceanic and Atmospheric Administration, U. S. Department of Commerce, and is entitled "Laboratory studies in mixing processes in estuaries and coastal flows on the Texas coast." Financial support facilitating the experiments conducted at the Institute for Hydromechanics at the University of Karlsruhe, Germany was awarded by the International Research and Education in Engineering Program (IREE) under National Science Foundation project number CBET–0637034.

I would like to thank my advisor, Dr. Scott Socolofsky, for his guidance and direction over the course of this project, and Dr. Kuang-An Chang and Dr. Robert Hetland for their support and input. Also, thanks to Duncan Bryant for collecting the laboratory data utilized for the analysis presented in this thesis.

Special thanks goes to Professor Gerhard Jirka at the Institute for Hydromechanics at the University of Karlsruhe, Germany, for allowing us to use the shallow water basin to conduct our experiments. In addition, I would also like to extend my gratitude to Wernher Brevis who was instrumental in teaching me how to operate the equipment. My experience in Karlsruhe is something I will never forget.

Finally, thanks to my parents and grandparents for their love and encouragement. Words can not describe how grateful I am to have them in my life.

TABLE OF CONTENTS

CHAPTER Page

LIST OF TABLES

LIST OF FIGURES

FIGURE Page

CHAPTER I

INTRODUCTION

Understanding tidal vortices is vital to estimate transport and flushing in an estuarine environment. The current status of knowledge on shallow water vortices is discussed in a brief literature review, and a description of how the research presented in this thesis intends to contribute information on vortices in a tidal application is provided. In addition, goals of the research are presented along with an outline detailing the remainder of the thesis.

A. Background

The formation and propagation of vortex dipoles play an important role in the flushing of estuarine regions. Estuaries depend on the transport of nutrients and sediments from the open sea to help maintain a prosperous environment. At the mouth of an inlet, tidal flow forces the formation of two vortices with opposite rotation, referred as the starting-jet dipole. These two dimensional vortical structures have lateral extents much greater than the water depth and are characterized as shallow flows. As the starting-jet vortices develop and flow through the inlet continues, secondary vortices shed due to separation from the inlet boundary, and eventually reach the starting-jet dipole. Starting jet vortices can either aid or hinder the transport of nutrients and sediment between these bodies of water. It is critical to understand the dynamics of this exchange because of the impact on water quality in the estuary and the role it plays in the life cycle of certain fish [3, 4, 5]. Without proper mixing, the circulation of fish larva from the sea to the estuary is impeded and the estuary can become

---

The journal model is Environmental Fluid Mechanics.

stagnant.

In recent years (for a more in depth literature review, see Nicolau del Roure et al. [18]), the evolution of jet generated vortex dipoles has been experimentally studied by Wells and van Heijst [22] and Afanasyev [2] using potential flow theory. Both used a thin layer of denser fluid to limit the 3D effects in order to approximate potential flow, and conducted the experiments using laminar flow. Wells and van Heijst determined a dimensionless parameter, referred to the inlet Strouhal number in this thesis, for Kashiwai's [10, 11, 12] vortex life histories which dictates whether a dipole will propagate away from the inlet on the reverse tide. Afanasyev conducted experiments to study dipole formation in steady flow. Utilizing the stratified system to approximate potential flow, no dependence on the depth of the fluid layers was observed in the results. A time scale referred to as the start up time was determined and indicates the time for a dipole to start propagating after an initial growth period. Afanasyev also implemented a simple model to estimate the start up time. However, it does not account for friction or the presence of walled boundaries and ultimately underestimates the result.

Unlike Wells and van Heijst and Afanasyev, the data presented in this thesis is turbulent flow and does not attempt to reduce 3D effects. As a result, the vortices decay due to bottom friction as they propagate away from the inlet. Similar bottom conditions were used for the data presented by Nicolau del Roure et al. [17, 18] which details the formation and propagation of tidal vortices through various inlet configurations. Nicolau del Roure et al. visualized the secondary vortices through dye studies, but the resolution of the data prohibited parameter calculations for these structures.

B. Problem Definition

Numerical models, such as the typical coastal numerical models ADCIRC, Delft3D or ROMS, use relatively coarse grids to resolve vortices. Although using a coarser grid minimizes computational time, small scale vortices can not be resolved. From previous dye studies, the secondary vortices have proven they are able to transport passive tracers and eventually these structures reach the starting-jet dipole. This thesis will explore the properties of the starting-jet dipole and the secondary vortices to determine relationships between the structures with the intent on eventually applying the experimental results to verify numerical models.

C. Objectives

This research is part of a larger Texas Sea Grant College Program project entitled "Laboratory studies in mixing processes in estuaries and coastal flows on the Texas coast" designed to examine the formation and propagation of tidal dipole structures and determine dynamics which quantify mixing. These results would be then be used to validate numerical models. To provide insight on the primary and secondary vortices, the following goals for this thesis are established.

- Hold the period and maximum velocity through the channel relatively constant to determine the influence of depth on all vortical structures.
- Identify and locate primary and secondary vortices in the flow using surface particle image velocimetry and the swirl strength.
- Write an identification and tracking program to calculate trajectory, equivalent diameter, vorticity, and circulation of vortices in the flow.
- Determine which flow characteristics impact vortex parameters.

- Relate the calculated properties of the primary and secondary structures to determine the impact of the secondary vortices on the starting-jet dipole.

D. Outline

Six chapters and two appendices compose this thesis. Beginning with Chapter I, a brief literature review is conducted and the scope and impact of the thesis research is examined. Chapter II describes the procedure for the experimental design and setup, while Chapter III chronicles the steps implemented to process the raw images obtained from the experiments and make them suitable for particle image velocimetry analysis. The automated code developed to assess the velocity vector fields obtained from particle image velocimetry is outlined in Chapter IV, and the analyzed output from the program is explained in Chapter V. In Chapter VI, conclusions and a summary are given for the presented research. Appendix A discusses related dye studies utilizing localized bottom roughness elements to damp the secondary structures, and the thesis concludes with Appendix B describing the movies included in the electronic supplement.

CHAPTER II

EXPERIMENTAL DESIGN AND SETUP

Experiments were modeled to correspond with natural conditions along the Texas coast. Three criteria were used in the development of the setup: Froude number, shallow water assumption, and the inlet Strouhal number. For the actual experiments, cameras where aligned above the inlet to capture the formation and propagation for half of the tidal dipole over multiple tidal cycles. The following sections will provide a detailed description of the experimental design and setup.

A. Experimental Design

Experiments were designed similar to those presented by Nicolau del Roure et al. [17, 18]. The criteria used to develop the experiments are outlined below.

1. Froude Number

The Froude number, Fr, is a ratio of the fluid speed to the speed of the waves and is shown in Equation 2.1

$$Fr = \frac{U_{MAX}}{\sqrt{gh}} \tag{2.1}$$

[13]. The variables in the equation are defined as: maximum velocity through the channel, U_{MAX}; water depth, h; acceleration due to gravity, g. The maximum velocity through the channel was chosen as the characteristic velocity for these experiments because the starting-jet dipole was sinusoidally forced by flow to imitate a tide. Depending upon the relation to the critical value of 1, two types of flow can ensue. If the Froude number is greater than 1, the flow is classified as supercritical, and subcritical if it is below 1. For the case when the Froude number is equal to 1, it is known as

critical flow. To scale the experiments to inlets along the Texas coast, a maximum Froude number of 0.20 was implemented [17, 18]. Although this is slightly high for natural flows, as long as the Froude number is low, the results will be independent of Froude number.

2. Shallow Water Assumption

Natural inlets are shallow and in order to apply the experimental results to models such as ADCIRC, the vortices must follow the shallow water assumption. This allows the inherently 3D structure of the vortex to be governed by the laws of 2D turbulence assuming the ratio of the lateral extent of the structure, λ, to the water depth, h, is much greater than 1, shown symbolically in Equation 2.2

$$\frac{\lambda}{h} \gg 1 \tag{2.2}$$

[8]. In addition, this assumption also assumes characteristics of the structure are depth-averaged and justifies the usage of surface velocity information.

3. Inlet Strouhal Number

A dimensionless parameter, referred to as the inlet Strouhal number, provides a method of predicting the fate of a dipole on the reverse tide given information on the inlet configuration and the flow through the inlet [22]. It is a function of the maximum velocity through the inlet, U_{MAX}, the inlet width, W, and the tidal period, T. The inlet Strouhal number, K_W, is shown below in Equation 2.3 equaling the critical value required for a dipole to remain directly in front of the inlet on the reverse tide.

$$K_W = \frac{W}{U_{MAX}T} = 0.13 \tag{2.3}$$

There are three options for dipole propagation during the reverse tide. A sta-

tionary dipole describes the condition where the dipole remains directly in front of the inlet on the reverse tide. When K_W is greater than the critical value, the dipole is entrained into the inlet. The other response is forward propagation, and this occurs when K_W is less than the critical value. The goal for the thesis experiments was to attain a stationary dipole to maximize data collection. However, the actual pump output resulted in stationary or propagating dipoles.

B. Experimental Setup

Experiments were conducted in the 15.0 by 5.5 meter shallow water basin at the Institute for Hydromechanics at the University of Karlsruhe, Germany. The laboratory at this location is ideal for studying environmental flows. One reason is that the shallow water basin has a smoothed surface to within $\pm$ 2 millimeters. In addition, the pumping system for the basin allows for sinusoidal forcing by flow, and the ability to reverse the flow direction. These specifications are optimal for investigating vortices in tidal flows.

To begin analyzing tidal vortices, the simplest configuration must first be considered. In the middle of the basin, an ideal symmetric inlet configuration was constructed, shown in Figure 1 with an inlet width of 0.79 meters. The inlet channel length is very small, 0.15 meters, to minimize the boundary layer. To mimic a tidal environment, the dipole was created by sinusoidally forcing flow through the inlet with a maximum velocity of approximately $0.20\frac{m}{s}$. After half of the tidal period, the flow was reversed using a system of valves. All of the experiments were administered using a 50 second tidal period for at least four consecutive tidal cycles. To maintain the shallow water assumption, experiments were conducted over water depths of 3, 5, and 9 centimeters.

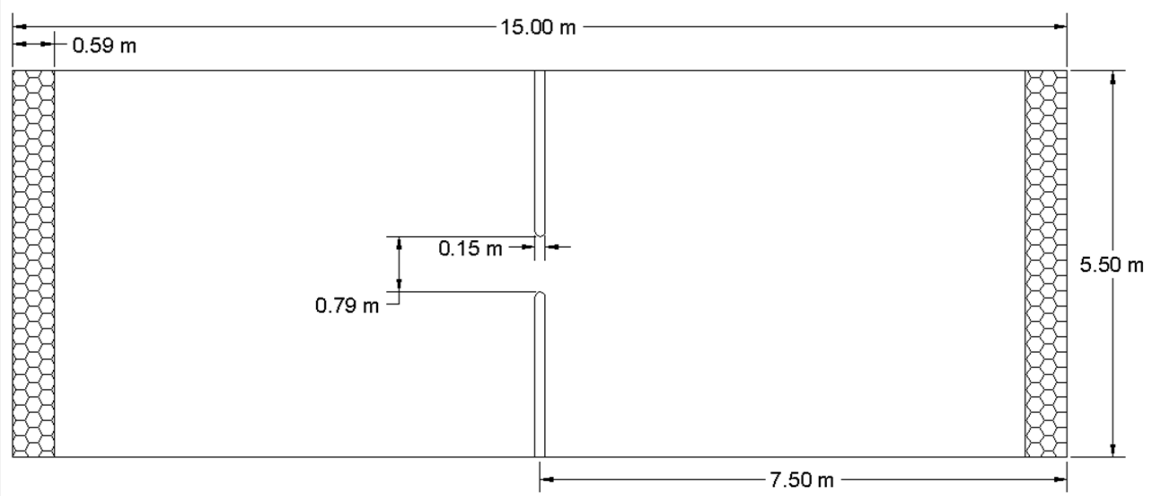

Fig. 1. Shallow Water Wave Basin Including Idealized Inlet Configuration.

Two CMOS cameras imaging at 16 Hz were mounted above the basin to capture the dipole formation and propagation on one side of the inlet. One camera was positioned with the field of view (FOV) shown in Figure 2; the other camera had a 10% overlap in FOV with the first camera and was situated downstream. Semi-buoyant tracer particles ranging from 2-3 millimeters were used to visualize the flow.

CHAPTER III

IMAGE PROCESSING

Using the raw images extracted from the CMOS cameras, surface velocities were obtained using particle image velocimetry in LaVision's DaVis software. First, the images needed to be pre-processed in Matlab to reach the conditions necessary to utilize particle image velocimetry. After the preliminary surface velocities were calculated, the vector fields were post-processed to minimize erroneous solutions and fill any holes in the data. Below is a detailed guide of the image processing techniques.

A. Pre-Processing

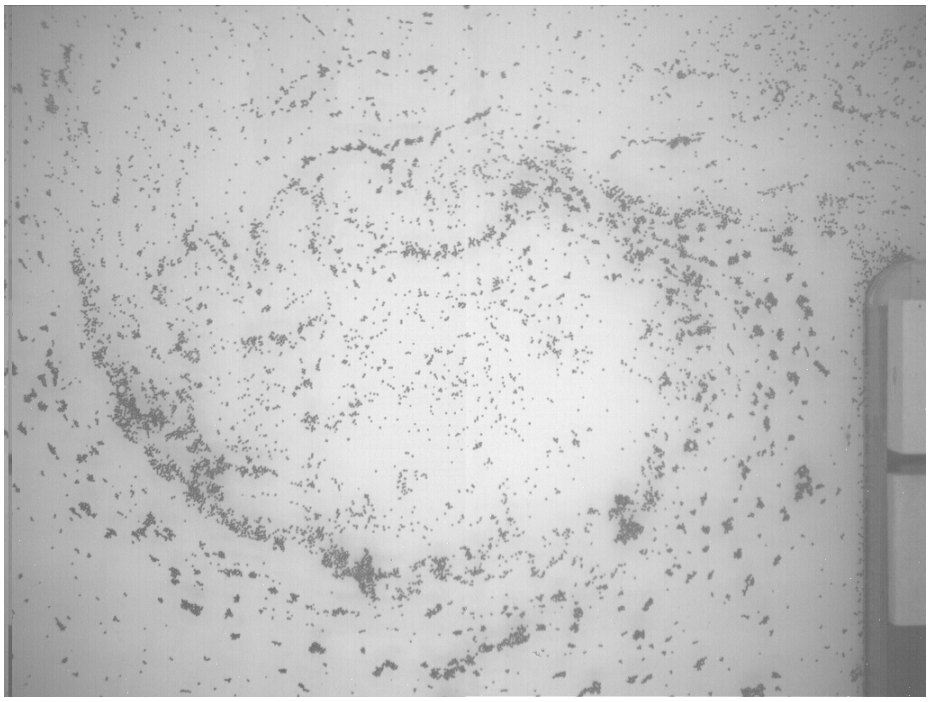

Fig. 2. Raw Image From One Camera.

The raw images collected from the CMOS cameras needed to be processed before being exposed to particle image velocimetry in LaVision's DaVis software. For particle image velocimetry to calculate velocities, it is necessary for the particles to be bright while the background is dark. The raw images contained black particles and a white background. One of the raw images from the experiments can be seen in Figure 2 with the inlet structure in the lower right hand corner.

As a result, the images were inverted using a gray-scale to provide the correct conditions to utilize particle image velocimetry. Once the images were inverted, a mean image was computed for each camera and was subtracted from all corresponding images in order to reduce reflections and background noise and provide more contrast. Figure 3 is the image as a result of this process and corresponds to Figure 2.

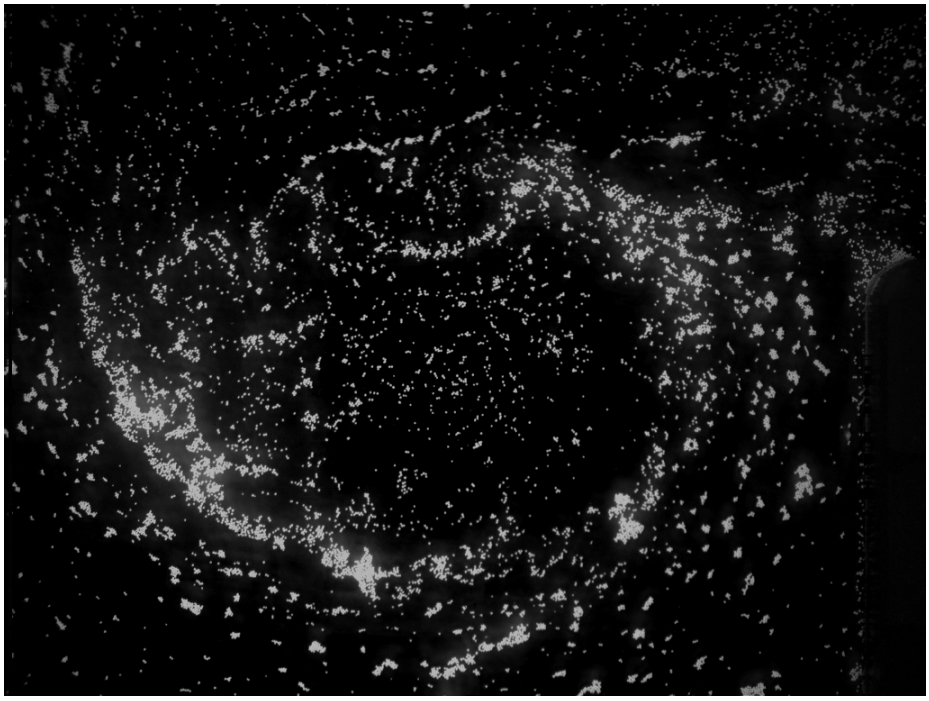

Fig. 3. Inverted Image With Mean Image Subtracted.

The images created as a result of image processing through Matlab were camera corrected using image processing in DaVis. Grid plate images with known distances between points were obtained from both cameras and used as a basis to correct for any distortion as a result of the camera lens. In the process, the images were also rescaled from pixels to millimeters in correspondence with the actual distance between the grid points. The cameras were mounted such that there was approximately 10% overlap in FOV and the grid plate extended the scope of one camera. Because the grid plate did not encompass the entire field of view of both cameras, images of the grid plate were taken with respect to each camera. One camera contained an image of the entire grid plate while the other camera only comprised of the 10% of the grid plate that extended into the neighboring field of view. Using these images, the left and right camera grids were aligned and cropped to yield a 64 pixel overlap, with confirmation from actual images. In order to guarantee the vectors in the overlap section of the field of view align, the outer edges of the image were cropped so that the number of rows and columns were divisible by 32, which corresponds to the final window selection for particle image velocimetry. Cropping and aligning the images occurred in Matlab. As a result, they needed to be rescaled in DaVis using the cropped grid plate images.

B. Particle Image Velocimetry (PIV)

Particle image velocimetry (PIV) uses the displacement of particles within a predefined area of observation and time step to calculate flow velocities. Before using PIV, the data must meet a number of criteria. First, the particle size in each image must encompass between 2-4 pixels. This allows for a gray-scale distribution of each particle to find sub-pixel resolution of particle locations. The selection of the interrogation

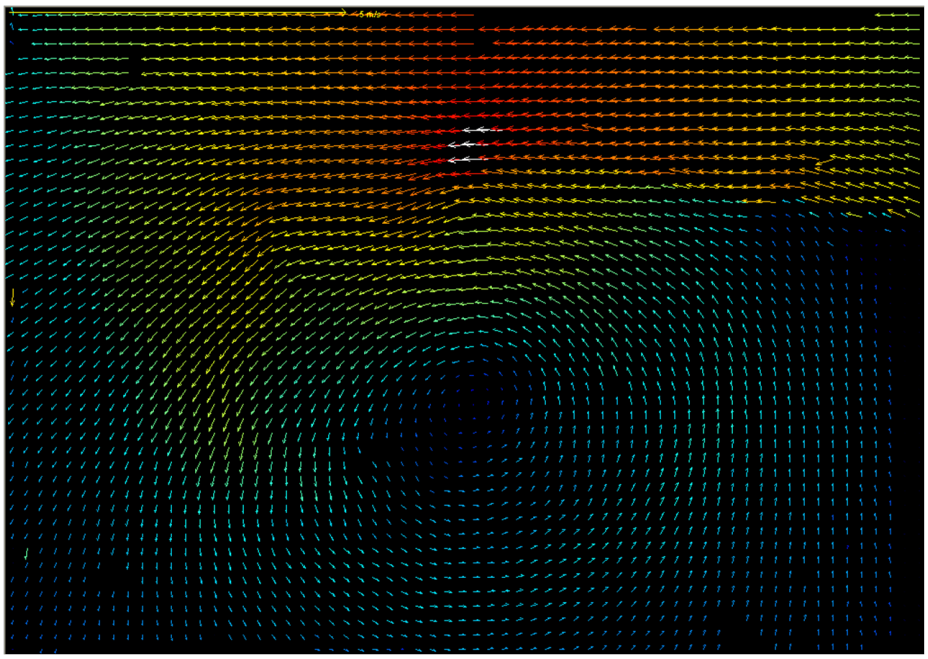

Fig. 4. DaVis PIV Output With the Size and Color of the Vector Indicating Intensity.

window size relies on the speed of the flow and the size of the structures desired for analysis. Choosing a window that is too small might allow the particles to move out of the field of view between frames, but selecting a window too large will cause less resolution for smaller structures. The size of the interrogation window is also compounded by the additional requirement of having at least 4-6 particles per interrogation window. Because PIV yields one vector per interrogation window, having more than a couple particles per window will decrease the likelihood of acquiring an erroneous solution.

Considering the requirements outlined above, cross-correlation PIV in DaVis was utilized to obtain surface velocity fields using successive images from each camera. Velocities were calculated with a multiple pass interrogation window at 50% overlap. The first iteration was conducted at the starting window size, 64x64 pixels, and two

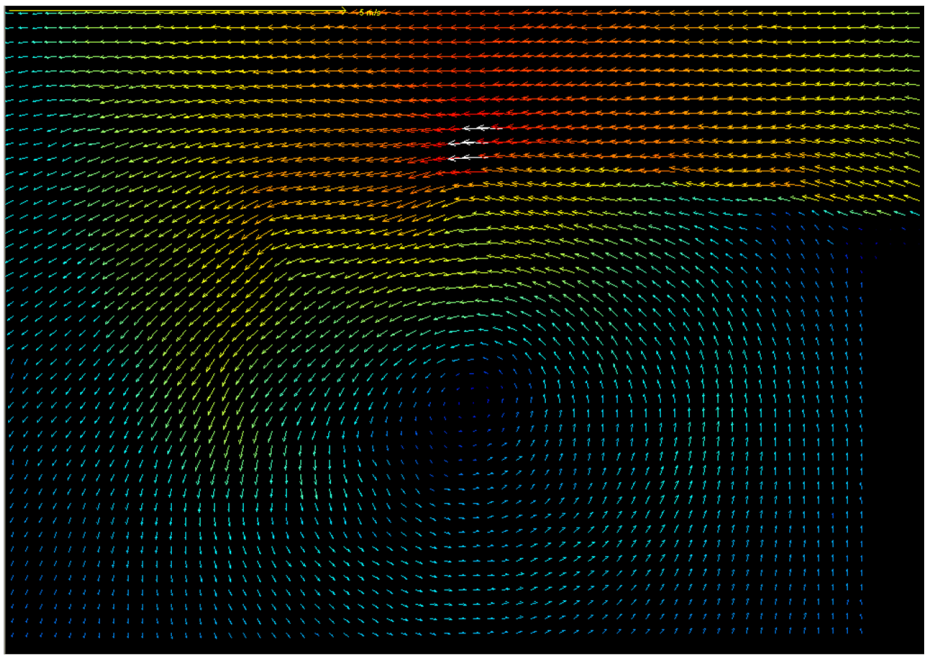

Fig. 5. DaVis Interpolated Output Including Inlet Mask With the Size and Color of the Vector Indicating Intensity.

iterations were completed using the final window at 32x32 pixels. The corresponding final PIV image is shown in Figure 4.

C. Vector Field Post-Processing

A median filter was applied to the velocity field in order to remove vectors that did not accurately represent the flow field. Using the eight surrounding data points, a mean vector was determined and it was compared to the center vector [14]. The data point was flagged if it was not within 0.1 times the root mean square of its surrounding data points or was among less than three vectors, and removed if its value was not within 0.3 times the root mean square of its neighbors. To ensure that data was not mistakenly calculated where inlet structures were present, a mask was

used. Data points within the mask were automatically set to zero. Due to insufficient seeding throughout the basin and the removal of error vectors, it was necessary to interpolate the data to calculate flow parameters. Missing data was inserted by evaluating the average of the non-zero surrounding vectors [14]. Both the median filter and interpolation were conducted using the DaVis software. The final image is shown in Figure 5. In this form, the images are ready to be applied to the vector field processing Matlab code which is described in Chapter IV.

CHAPTER IV

VECTOR FIELD PROCESSING

An automated Matlab code was developed to process the copious amount of data obtained from the experiments. The left and right vector maps for one time step are read into the program. Once all calculations are completed and the current data is stored into the correct variables, the left and right vector maps for the next time step are entered into the program and the process repeats. After the program finishes analyzing the last set of vector maps in the data set, the secondary vortex variables, known as the global variables, are saved as Matlab data files in the current folder. The saved output is then manually examined for secondary vortex information, and non-dimensionalized using the tidal excursion and its components.

A. Reading in Data

The process begins by deleting the header at the beginning of the DaVis output text files using code obtained from Dong Guan Soel. Next, the position and velocity data for each vector is extracted and recomposed into distinguishable variables. Horizontal and lateral distances and velocities are stored as their own parameters, however, a universal spatial zero setting is not determined at this point. During this step, grid distances between the vectors are also computed based upon the loaded data.

B. Combining Camera Images

The next m-files combine variables from the left and right cameras into one variable corresponding to the type of data it yields. As described in Chapter III, the left and right camera images are cut to include a 64 by 64 pixel overlap for PIV analysis.

All of the resulting overlap data is discarded for the right camera variables, while variables for the left camera eliminate common data with the right camera and retain the information corresponding to the "seam" between the vector maps. Figure 6 illustrates an instantaneous vector field with every other vector removed to provide clarity and the red vertical lines indicating the grid spacing for the seam vectors. The field of view is truncated in this image to accentuate the vortex formation. With

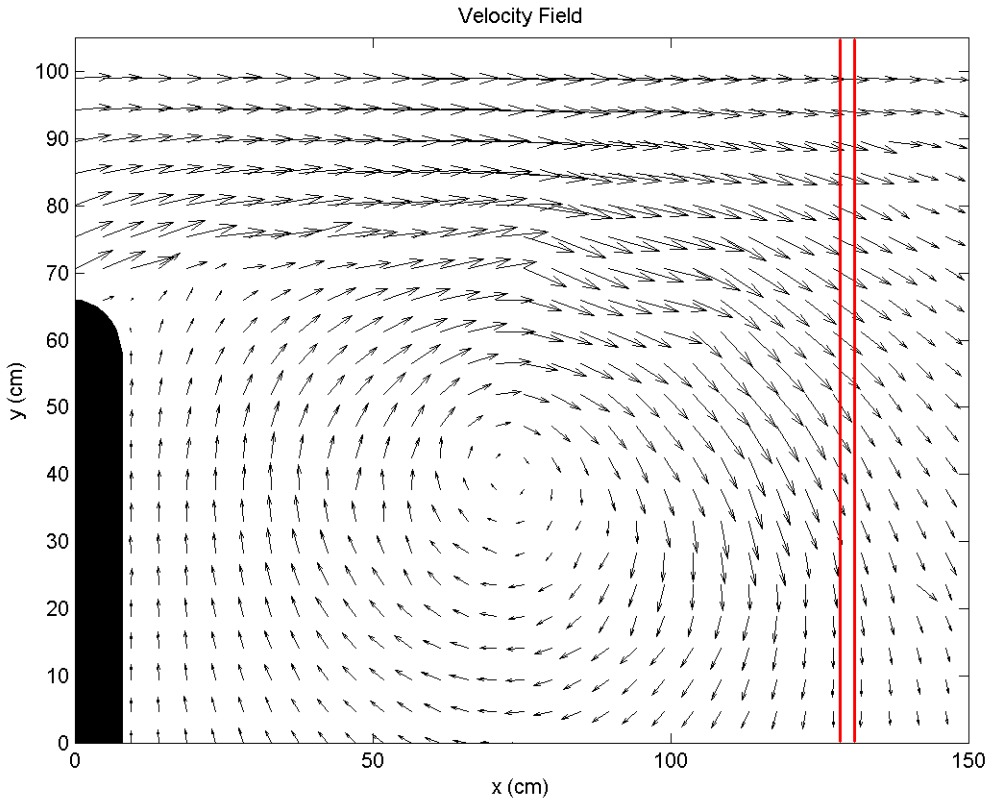

Fig. 6. Velocity Vector Field With Every Other Vector Removed.

the collective data, the spatial zero is temporarily set to the bottom left corner of

the image, and the instantaneous velocity through the channel is measured using an average of the vectors within the channel.

C. Determining Spatial Derivatives of Surface Velocities

Once the left and right vector maps are combined, the spatial derivatives of the surface velocities are calculated. This code has the ability to compute the derivatives utilizing a number of techniques. The method selected for this analysis was the central difference

$$\left(\frac{df}{dx}\right)_i \approx \frac{f_{i+1} - f_{i-1}}{2\Delta x} \tag{4.1}$$

[19]. As shown in Equation 4.1, the central difference uses the point behind and the point in front of the current data point to compute the derivative yielding a second order accurate solution. This form of finite difference works as a method of moderate smoothing, which helps reduce the influence of error vectors. Other options for determining the derivatives are the forward difference and least squares method. The forward difference is a first order accurate solution which uses the current and proceeding point to compute the derivative, presented in Equation 4.2

$$\left(\frac{df}{dx}\right)_{i+1/2} \approx \frac{f_{i+1} - f_i}{\Delta x} \tag{4.2}$$

[19]. Using this method of two point computation, the data is not smoothed and any error vectors present are likely to have great influence on the outcome. On the other extreme, the least squared method, displayed as Equation 4.3, uses five points (two proceeding, two behind, and the current) to produce a derivative

$$\left(\frac{df}{dx}\right)_i \approx \frac{2f_{i+2} + f_{i+1} - f_{i-1} - 2f_{i-2}}{10\Delta x} \tag{4.3}$$

[19]. Because the calculation uses more points, the data becomes smoothed and will greatly reduce the influence of error vectors; however, it may aid in over-estimating the size of the vortex structure since derivatives are employed for vortex identification.

D. Object Identification

Identification of vortices is based upon the swirl strength criteria proposed by Adrian et al. [1]. Spatial derivatives of the horizontal and lateral flow components, u and v respectively, are used to formulate the two-dimensional deformation tensor D^{2D} as

$$D^{2D} = \begin{pmatrix} \frac{\partial u}{\partial x} & \frac{\partial u}{\partial y} \\ \frac{\partial v}{\partial x} & \frac{\partial v}{\partial y} \end{pmatrix}. \tag{4.4}$$

The swirl strength is calculated by identifying the positive imaginary eigenvalues of Equation 4.4. These points correspond to areas where there is local rotation, and no contamination by local strain is present as would be for the vorticity. Figure 7 is the corresponding swirl strength contour for the velocity vector map presented in Figure 6 and proves the swirl strength is an excellent method for locating vortices that are not readily visualized in the velocity vector field. In addition to the primary vortex, Figure 7 identifies two secondary vortices from x=0 to 50 centimeters, one directly above the swirl strength peak of the main vortex, and at least two others beginning to rotate around the main vortex. The secondary vortices which move past the horizontal location of the swirl strength peak of the main vortex are defined as satellite vortices because they orbit the main vortex. In this thesis, the contiguous swirl strength contours associated with the combination of the main vortex and the satellite vortices is referred to as the vortex system.

Vortices are located based on regions of contiguous swirl strength, and do not include swirl strength within the inlet channel. The program finds all objects in the

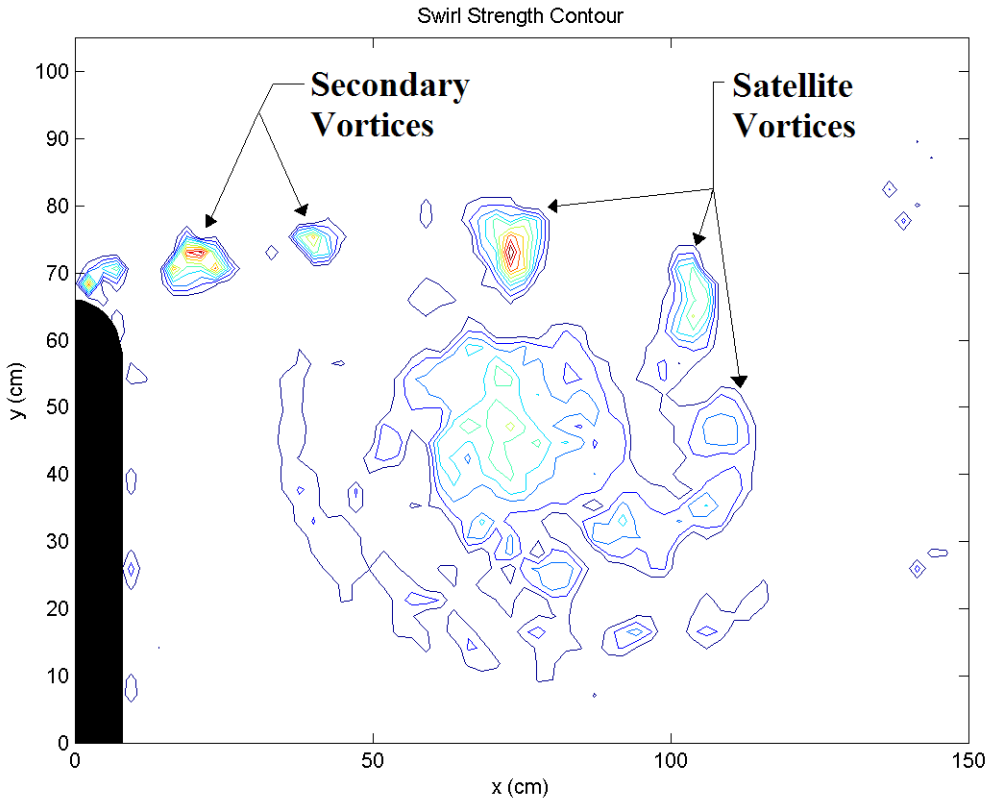

Fig. 7. Swirl Strength Contour.

image above a predetermined noise level. If no objects are found, the next pair of images is entered into the code. When objects are discovered, the program determines which object is the largest using a size threshold of at least three grids to declare an object the main vortex. In the event of two objects having the same size, the main object becomes the one with the higher maximum swirl strength. The centroid and location of maximum swirl strength of all objects are found and stored for later use. However, if the main vortex is out of the field of view to the right hand side, calculations terminate and the next pair of images is entered into the program.

The location of maximum swirl strength for the main vortex corresponds to the center of rotation for half of the vortex dipole. Occasionally, this point is initially misidentified due to incoming secondary vortices, whose maximum swirl strength is relatively larger, adhering to the swirl strength of the main vortex. To inspect if this point is correctly located, 50% of the maximum swirl strength of the main vortex and above form another variable. Iteratively, the code examines the main object for peaks using increasing percentages of the initial maximum swirl strength to redefine the object. If only one peak is found, the program continues to the next iteration. If another peak is detected, the location of maximum swirl strength is identified. Maximum swirl strength locations are stored at the end of each iteration and compared to eliminate double counting. The maximum swirl strength of the main vortex is defined as the peak closest to the calculated centroid.

For other objects initially identified in the image, the minimum size of each object must be greater than one grid; otherwise, the item is deleted because it can not be adequately resolved. Next, the centroid of each object is compared to the location of peak swirl strength for the main vortex. If the object is horizontally past this threshold, it can be considered part of the vortex system since its trajectory is influenced by the dipole at this time. Similarly, if the object is laterally located below the main vortex peak, it can also be part of the system. All objects that fail these criteria are labeled as secondary vortices. It is important to note that no criterion is set for horizontal location before the swirl strength peak of the main vortex. Objects already orbiting around the primary vortex can be mislabeled as secondary vortices. When the output is manually analyzed these erroneous objects can be extracted based upon their curved trajectory around the primary vortex. Finally, the vortex system is checked to determine if it is in the FOV; if it is not, all computed variables for the vortex system become zero except the location of the maximum swirl strength.

E. Parameter Calculations

For the vortex system and the identified secondary vortices, the centroid is used to track the trajectory. In addition, the equivalent diameter, vorticity at the swirl strength peak and circulation are computed for each object. Because the vortices seem to retain their circular shape, the rotational area for each object is treated as a circle to approximate the diameter of each vortex. The vorticity, ω, is calculated based upon spatial derivatives of the flow components, and the circulation is computed with

$$\Gamma = \int_A \omega dA. \tag{4.5}$$

These parameters are stored in variables which span the entire length of the data set, and their position within the variable matrix is determined by the vortex tracking code.

F. Vortex Tracking

Properties calculated for the vortex system are contained in row vectors with each column representing the values for that specific time step. Large matrices are designated to save information for the secondary vortices. Data is logged according to variables; with the same position within the matrix corresponding to one instantaneous secondary vortex, each row representing a time step, and columns signifying the history of one vortex. The first time secondary vortices are detected, properties for each object are placed in the row representing the time step in which they are located with the object yielding the highest swirl strength in the first column, second highest in the second column, etc., until all of the object parameters are saved. For subsequent images, the equivalent diameter and centroid of vortices present in the previous time step are compared with those found in the current time. Current ob-

jects are ordered in decreasing magnitude of swirl strength. Starting with the first, the centroid of each object is compared with the centroid of each previously located secondary vortex. If the distance between centroids of the current and previous vortices is less than the radius of the previous vortex, it is considered the same object and properties are stored in the column assigned to that vortex in the row symbolizing the current time. If multiple vortices are located within the radius of a previous vortex, the object with the larger equivalent diameter prevails. Once a vortex is tracked into the current time step, it is no longer available for comparison to other vortices. When a currently defined vortex does not meet the criteria for a previously located mate, values are stored in the next available column. As a result, the code has the ability to track life and death of vortices. If values are not recorded for the previous time step, the program takes the next available column and stores the objects implementing the same procedure for placement as when the secondary vortices are initially identified. Vortex properties for the vortex system and secondary vortices are saved in the current folder once the vector maps for the final time step have been processed.

G. Non-Dimensionalization

Once the secondary vortex information is selected from the output variables, both the secondary vortex and vortex system data is non-dimensionalized by the average maximum velocity through the channel, U_{MAX}, the average tidal period, T, and the tidal excursion which is equal to

$$TidalExcursion = \frac{U_{MAX}T}{\pi} \tag{4.6}$$

[15] and is the distance a particle can travel during one tidal cycle. A list of the non-dimensional variables is shown in Table I.

Table I. Non-Dimensional Parameters for Vortex Characteristics.

Dimensional Variables	Non-Dimensional Variables
X	$X^* = \frac{X}{U_{MAX}T}\pi$
Y	$Y^* = \frac{Y}{U_{MAX}T}\pi$
ω_{peak}	$\omega^* = \omega_{peak}T$
Γ	$\Gamma^* = \frac{\Gamma}{U_{MAX}T}\pi$
D	$D^* = \frac{D}{U_{MAX}T}\pi$
t	$t^* = \frac{t-t_{start}}{T}$

Experimental data was normalized using the beginning of the first tidal cycle. For the time variable, t_{start} is the elapsed time between the start of the experiment and the beginning of the respective tidal cycle.

CHAPTER V

RESULTS AND DISCUSSION

Once all of the parameters were calculated for the vortex system and secondary vortices, relationships between each individual characteristic and changes in maximum velocity through the channel and depth were identified. To quantify the role of friction in the experiments, a friction stability analysis was conducted. Consistency among the tidal cycles was examined for the vortex system data and secondary structures born at the same time during the third tidal cycle were compared.

A. Vortex System

Beginning at the time when flow initially moves through the inlet, the "spin up" time is defined as the time elapsed before the independent recognition of the secondary vortices separate from the primary vortex. Table II lists the average spin up time for the primary vortex in each experiment with respect to the average measured tidal period.

The spin up time for the 9 and 3 centimeter experiments are roughly similar while the 5 centimeter water depth primary vortex has a shorter developmental stage.

Table II. Measured Average Spin Up Times and Inlet Strouhal Numbers.

Experiment	Spin Up Time	K_W
9 cm	0.22T	0.08
5 cm	0.17T	0.06
3 cm	0.23T	0.09

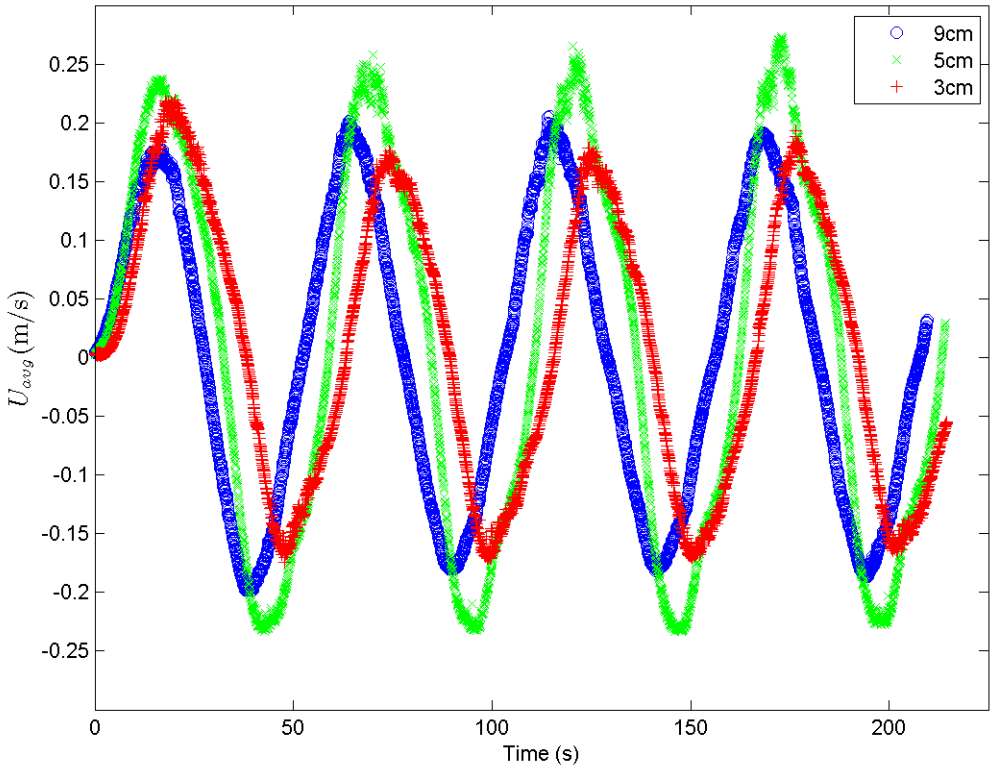

Fig. 8. Average Velocity Through the Channel.

Examination of the average measured velocity through the channel, illustrated versus time in Figure 8, shows the average velocity is higher for the 5 centimeter experiments, which contributes to the lower spin up time. Similarly, the average velocity for the 3 centimeter experiment is the lowest and corresponds to a longer spin up time. The similar spin up times for the 9 and 3 centimeter water depth cases are likely due to their relatively similar maximum velocity through the channel.

Another point to consider when analyzing the average measured velocity, U_{avg}, plot is the effect of bottom friction on the first tidal cycle. Because the experiments

Table III. Friction Analysis.

Experiment	S_f	$l_f\,(m)$
9 cm	0.0623	6.34
5 cm	0.1343	2.94
3 cm	0.2581	1.53

started in a placid basin, there is no momentum present from the previous tidal cycle. Therefore, the initial phase lag increases the shallower the water depth because there is more bed friction to overcome. After the first cycle, the original phase lag seems to remain constant. Since the first cycle does not accurately describe the flow conditions for the remainder of the experiment, it has been omitted from all experimental results reported in the remaining sections of this thesis.

To further explain the influence of bottom friction on the experiments, a frictional stability analysis was conducted and is displayed in Table III. The frictional length scale, l_f is $\frac{h}{2c_f}$ [20] and the bed friction parameter, S_f, is defined as $c_f\frac{W}{h}$ [21] where c_f is a quadratic-law bed friction coefficient, W is the inlet width and h is the water depth. Obviously, the effect of friction plays a different role with each experiment. As expected, the frictional length scale increases with water depth. According to Chen et al. [6] for shallow wakes the critical bed friction parameter required for the onset of stabilization is 0.18, and this value falls somewhere between the 5 and 3 centimeter experiments. As a result, consideration of friction is important when analyzing the experimental results, especially for the 3 centimeter water depth case. Because friction will greatly influence the 3 centimeter water depth case, it is expected to yield more damping and less energetic secondary vortices.

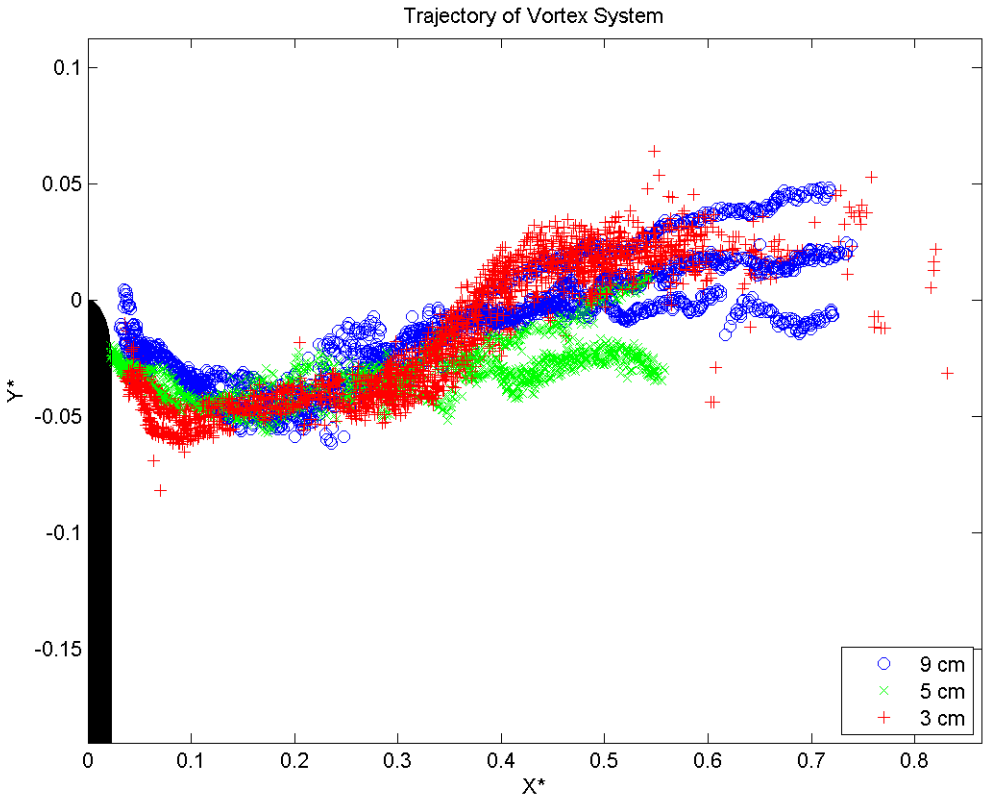

Fig. 9. Non-Dimensional Trajectory of the Vortex System Centroid for the Second, Third and Fourth Tidal Cycles.

In addition to spin up time, the relatively higher velocity for the 5 centimeter experiment also justifies the difference in the vortex system trajectory among the water depths. Table II also lists the calculated inlet Strouhal number for each experiment. The criterion for a stationary vortex is 0.13, and all of the calculated inlet Strouhal numbers are below this value which indicate propagating vortices on the reverse tide. Figure 9 provides a non-dimensional plot of the vortex system trajectory using its centroid location to plot the data points. The data for each cycle is in good agreement for each experiment. A common trend for the vortex system over

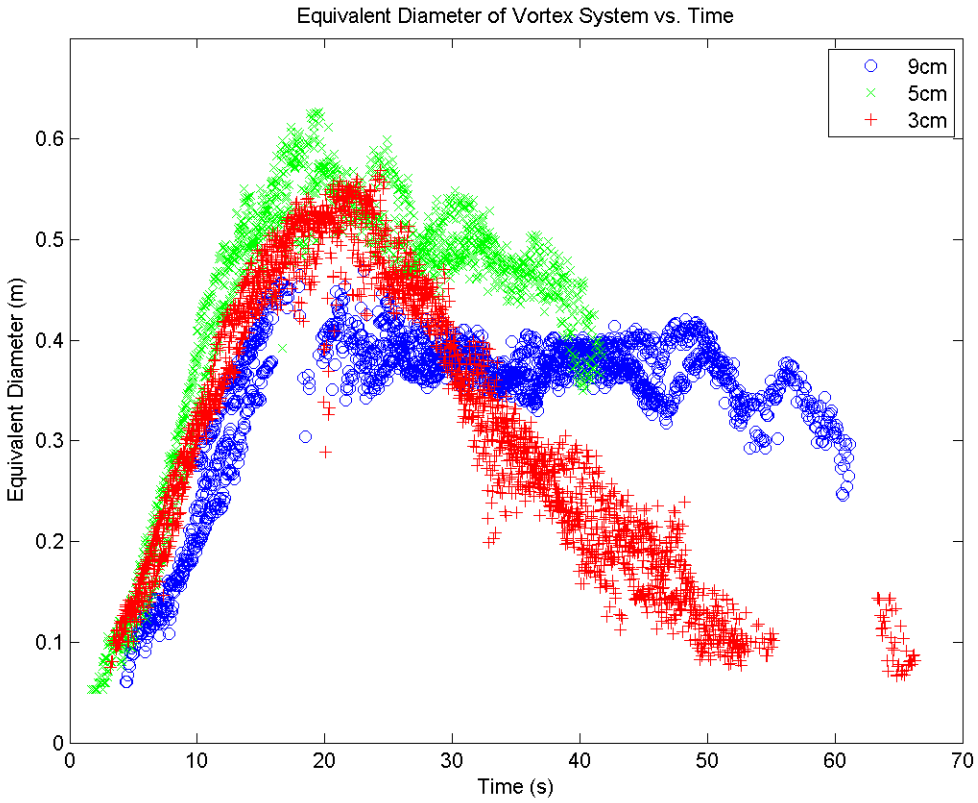

Fig. 10. Diameter of the Vortex System Versus Time.

all the tested water depths is an initial migration away from the center of the inlet. Once the tide turns, the dipole contracts and the primary vortices move back toward the center of the inlet. Corresponding with the inlet Strouhal number in Table II, the scatter in the points for the 3 centimeter experiment can be attributed to the near stationary vortex status while the lines of the 9 and 5 centimeter experiments indicate more of a propagating vortex on the reverse tide. As a result of its stationary condition, the primary vortex for the 3 centimeter experiment is stretched and pulled apart by strain as the tide reverses while the 9 and 5 centimeter systems seem to

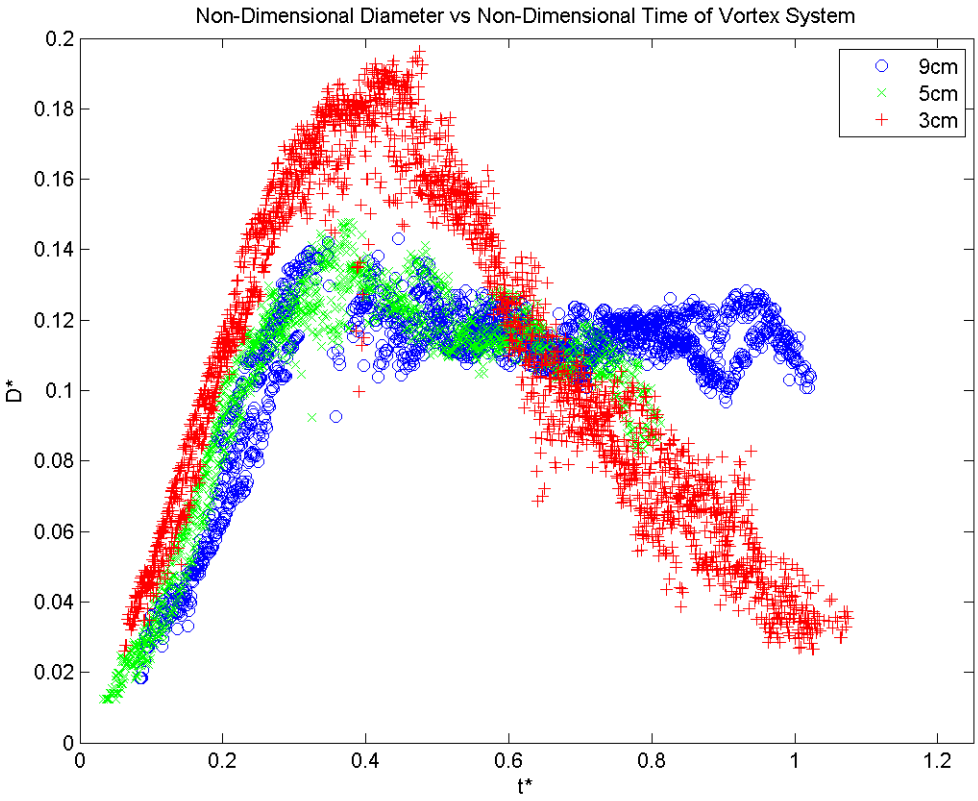

Fig. 11. Non-Dimensional Diameter of the Vortex System Versus Non-Dimensional Time.

only slightly decrease in size on the reverse tide and decay less dramatically over time as shown dimensionally in Figure 10. It is also important to note that the peak of the 3 centimeter system diameter is nearly the same magnitude as the 5 centimeter water depth experiment, which is not expected since the magnitude of the maximum velocity through the channel is more similar to the 9 centimeter water depth case. Illustrated in Figure 11, when non-dimensionalized by the tidal excursion the diameter for the 5 and 9 centimeter water depths collapse while the 3 centimeter depth case is artificially high. Due to frictional effects, the 3 centimeter vortex system does

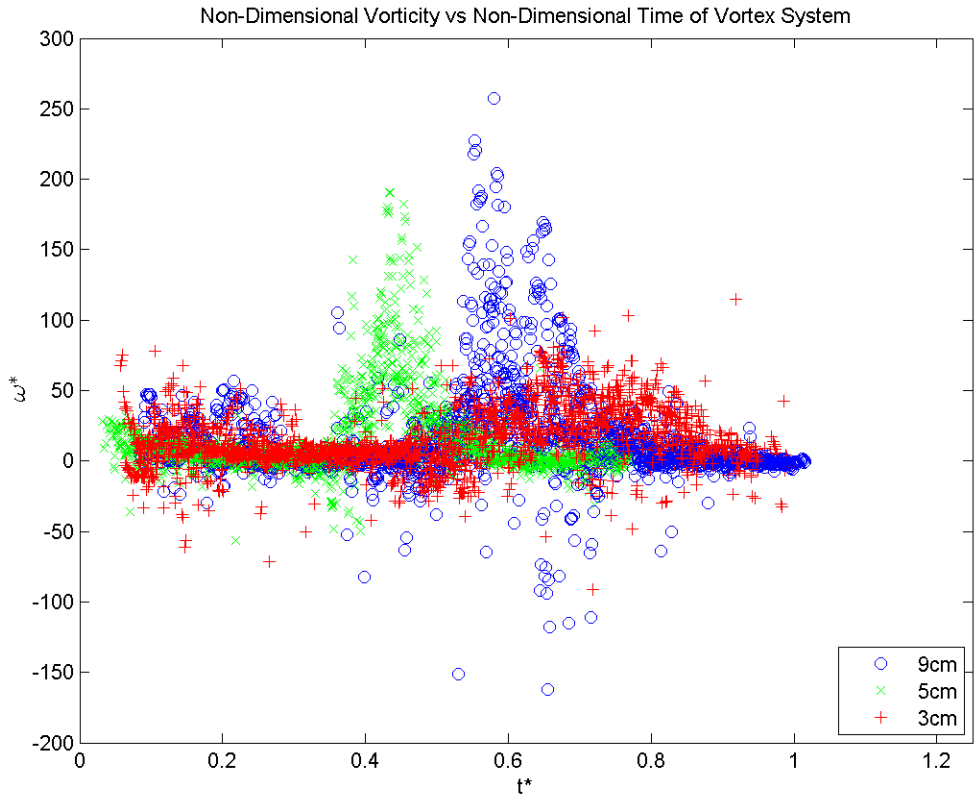

Fig. 12. Non-Dimensional Vorticity at the Swirl Strength Peak for the Primary Vortex Within the Vortex System Versus Non-Dimensional Time.

not form a cohesive unit during spin up (visualized in the movies in the electronic supplement). Usually, the primary vortex is composed of many smaller vortices which get wrapped up into a core during the spin up. The 3 centimeter depth experiment never really forms the vortex core; instead, it is a composite of many small vortices which leads to the excessive growth and the dramatic decay of the vortex system for this experiment.

In addition to diameter, the vorticity at the swirl strength peak was also calculated for the primary vortex within the vortex system and is portrayed in Figure 12

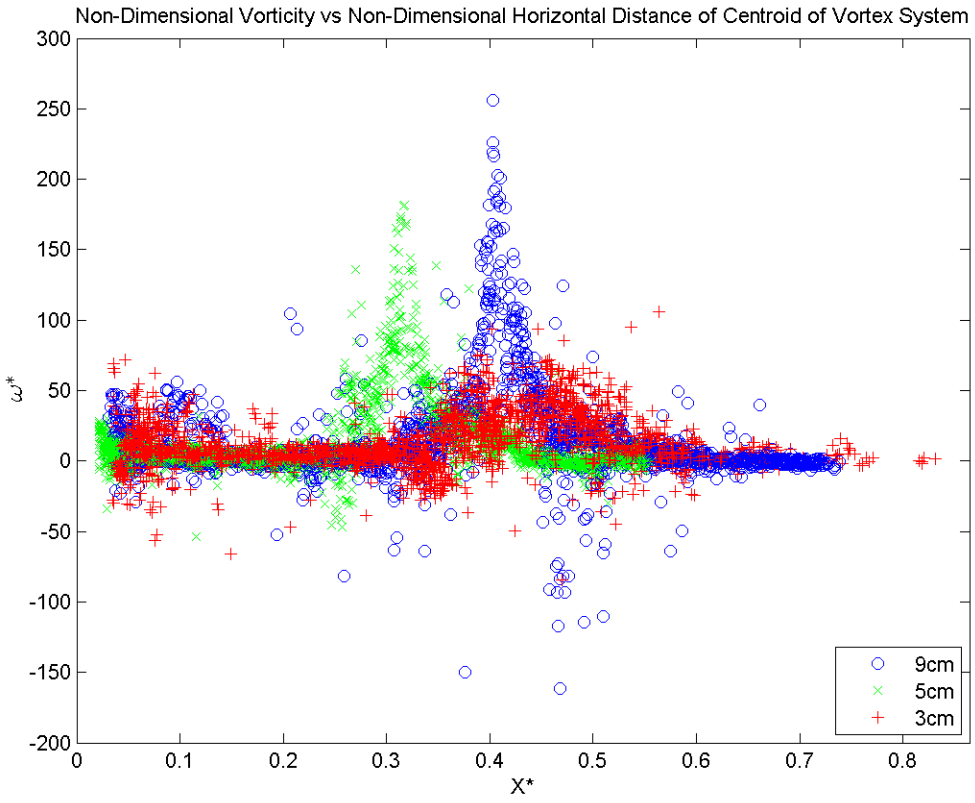

Fig. 13. Non-Dimensional Vorticity at the Swirl Strength Peak for the Primary Vortex Within the Vortex System Versus Non-Dimensional Horizontal Location of the Centroid.

versus non dimensional time. The swirl strength peak of the primary vortex corresponds to the center of rotation for half of the starting-jet dipole. At approximately half of the tidal cycle, there is a large spike in the vorticity for all three experiments. When the tide reverses, flow circumnavigates the dipole in its quest to arrive back at the inlet. In the process, it acts to supplement the spin of the primary vortices. There are also points indicating negative vorticity. Although the starting-jet dipole is considered to be 2D, there is a 3D turbulent background flow. No attempts were

made in the experimental design to damp the 3D instabilities associated with these vortices. Hence, turbulence is generated as a result of bottom friction and may be upwelled through the primary vortex core which helps to explain the erratic nature of the vorticity calculations.

A possible attribution for the deviation in vorticity peaks is the nonconformity of velocity through the channel among the experiments. The velocities for the 9 and 3 centimeter water depths are comparable and vorticity peaks for these experiments fall about the same time during the tidal cycle. Therefore, there is indication that the maximum velocity through the channel influences the temporal properties of the vortices. Since the maximum velocity values for the 9 and 3 centimeter experiments are small relative to the 5 centimeter, the initial velocities on the reverse tide are smaller in magnitude causing a delay in the response of the vortex system on the reverse tide, which is also reported spatially in Figure 13. Like the temporal plot of vorticity at the swirl strength peak of the primary vortex, its corresponding spatial plot also shows variations in the vorticity peaks due to the maximum velocity through the channel with experiments exhibiting greater maximum velocities yielding vorticity peaks closer to the inlet.

Similarly, for the circulation plots in Figure 14 and Figure 15 there are also notable differences in the temporal and spatial location of the peak between the tested water depths. Locations are consistent with the observations of the downward cascade of maximum velocity values causing increasing temporal and spatial locations of the peak circulation. Within each experiment, the circulation peaks seem to fall consistently in the same horizontal location. Circulation peaks occurring early in the tidal cycle are due to the influence of secondary structures from the latter half of the previous cycle becoming entrained into the inlet as the tide reverses and influencing the development of the primary vortex. This is particularly true for the 3 centimeter

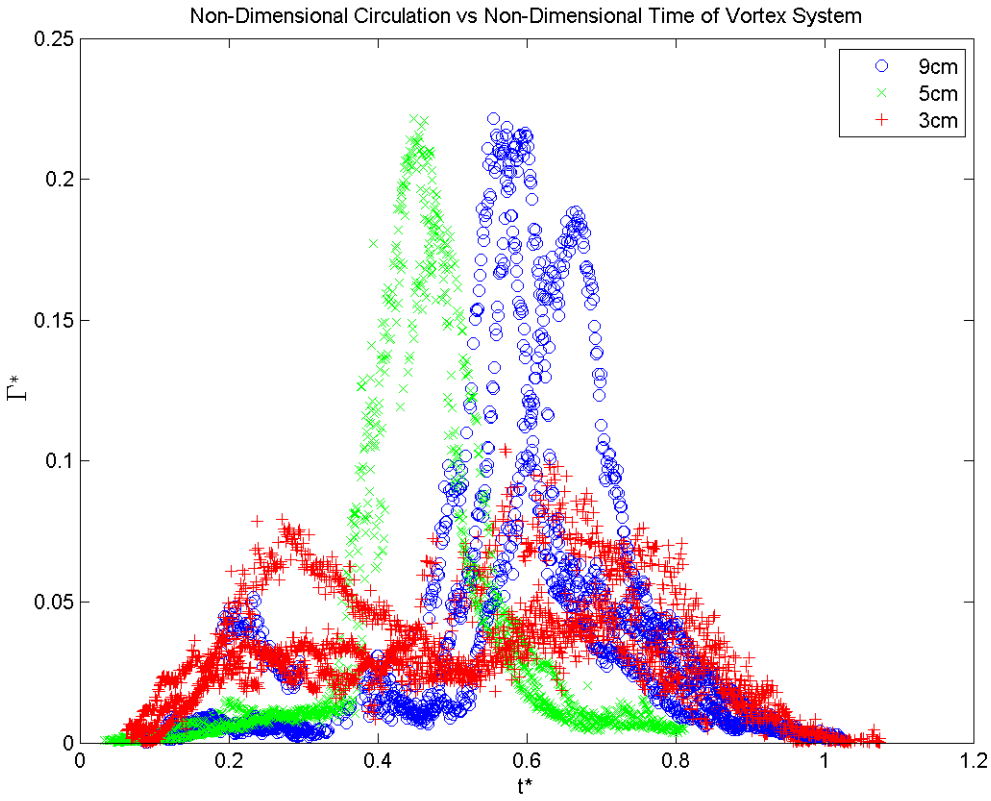

Fig. 14. Non-Dimensional Circulation for the Vortex System Versus Non-Dimensional Time.

water depth case since more structures are transferred between tidal cycles as a result of the smaller propagation distance of the dipole before the tide reverses (see the swirl strength movie of the 3 centimeter experiment with attention on the 4th tidal cycle).

B. Secondary Vortices

Unlike the vortex system, the secondary vortices proved more difficult to track. The noise level selected for the swirl strength metric is too low to completely separate vortices if they are in close proximity to one another. This is particularly true when the

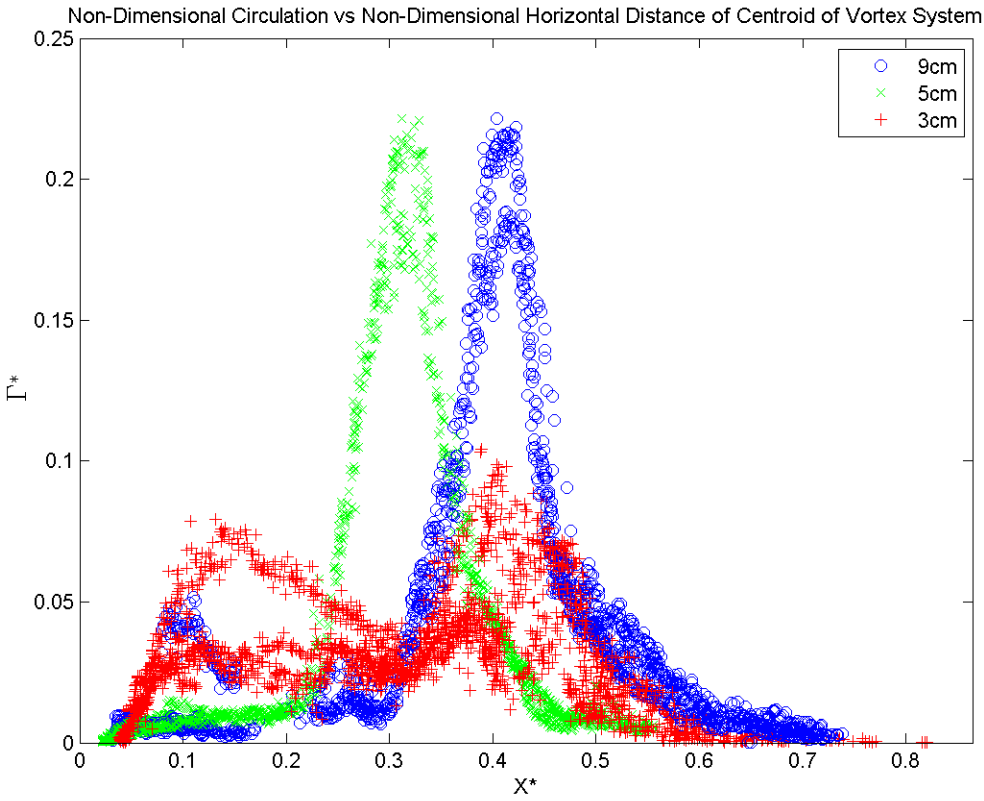

Fig. 15. Non-Dimensional Circulation for the Vortex System Versus Non-Dimensional Horizontal Location of the Centroid.

vortices are close to the inlet—immediately after they are born—or almost entering the vortex system. Figure 16 is a plot of an instantaneous object identification and its corresponding swirl strength. The magenta square indicates the location of the swirl strength peak while the green square represents the calculated centroid for the vortex system. The swirl strength clearly shows an object with two swirl strength peaks about to enter the vortex system near x=20 to 40 centimeters. The area of swirl strength connecting these two peaks can be attributed to the combination of the surfacing of 3D instabilities and the result of some uncertainty due to the spa-

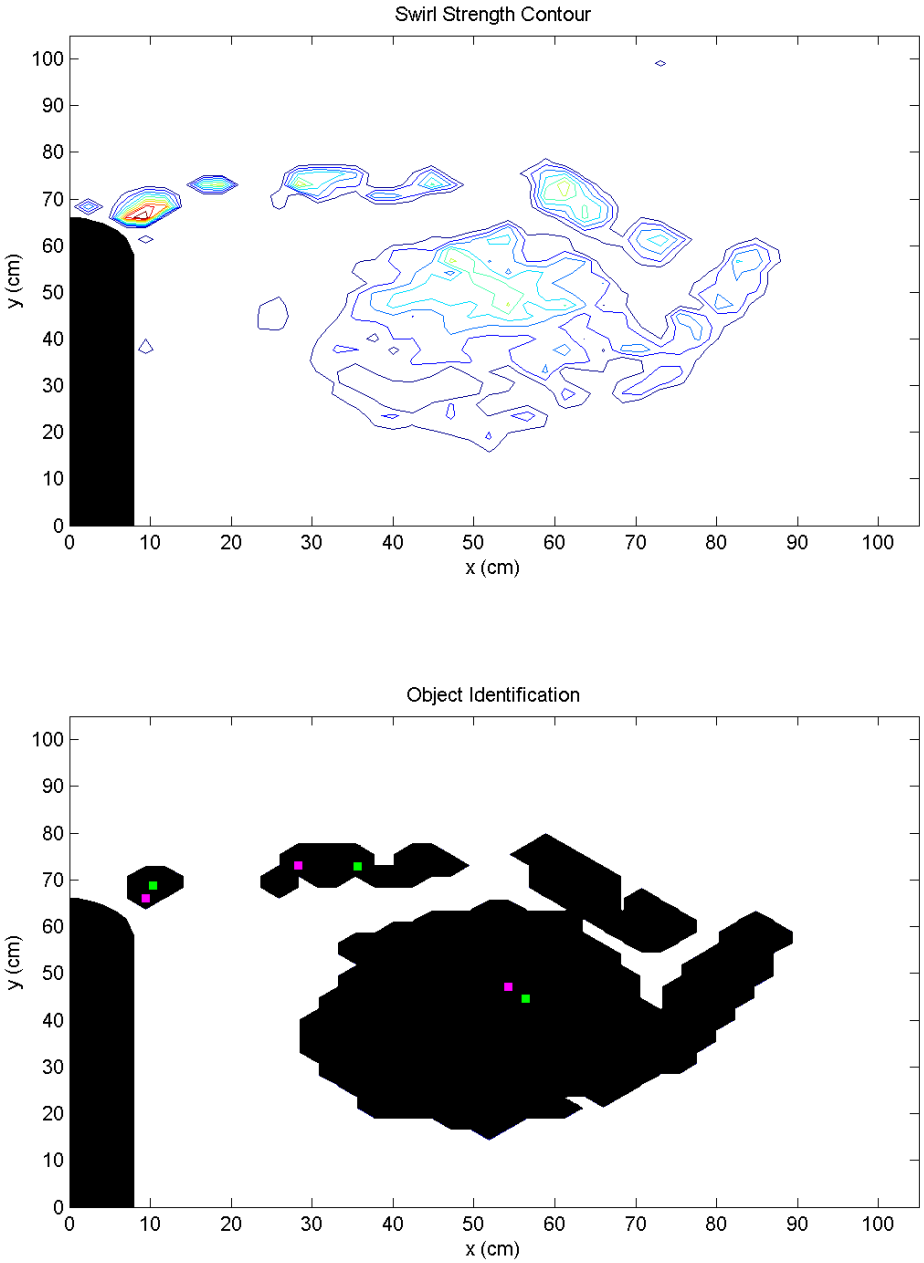

Fig. 16. Error in Instantaneous Object Identification and Corresponding Swirl Strength During the Second Tidal Cycle of the 5 Centimeter Water Depth Experiment at Time=0.36T Into the Tidal Cycle.

tial resolution of the PIV data. Unlike the vortex system, the size of the secondary structures is approximately the same order of magnitude as the water depth. As a result, the bottom friction has a greater effect on the secondary vortices, causing 3D instabilities to surface. The relatively small size of the secondary vortices also poses some uncertainty since the grid size for the PIV vectors are also on the same order as the water depth and approximately the same order as the size of the secondary vortices. Therefore, there are a limited number of vectors used to resolve the secondary structures and the resolution contributes to the problem of separating the 3D turbulence from the secondary vortices. The 3 centimeter water depth experiment is especially effected by this flaw in the code because the dipole does not travel far from the inlet.

Figure 17 illustrates the secondary vortices identified by the vortex tracking code and their respective birth times within the third tidal cycle. The theoretical slope of the number of secondary vortices versus time is shown with the solid lines color coded to represent each experiment. Theoretical values were calculated using the radius of curvature of the inlet ends, the average maximum velocity through the channel, and a Strouhal number equal to 0.2. Because it is tidal flow and the secondary vortices are not independently recognized from the dipole at the beginning of the cycle, there is some question as to which data points, if any, the line should go through. To provide a better visualization of the formation of the secondary vortices with respect to the characteristic flow conditions, the theoretical slope of secondary vortex shedding is illustrated using the first identified secondary vortex in each experiment as the starting point. According to the equation for the Strouhal number, the secondary vortex frequency should be similar for the 3 and 9 centimeter cases due to comparable maximum velocities through the channel. As confirmed by the swirl strength movies, the number of secondary vortices located by the code for the

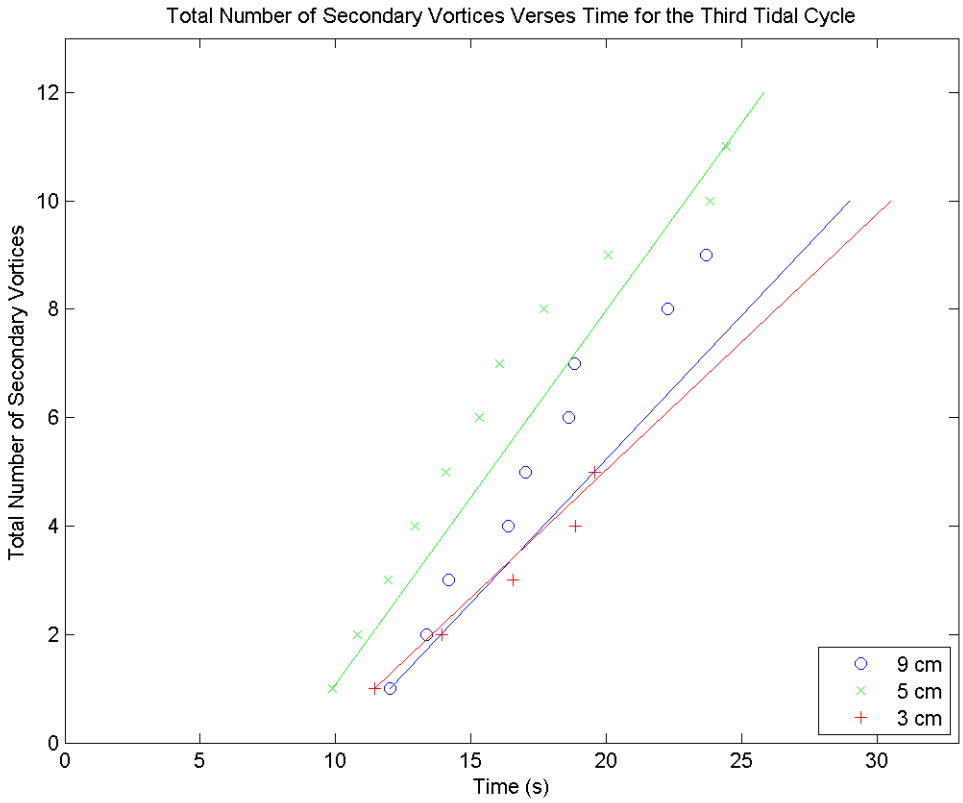

Fig. 17. Number of Secondary Vortices Identified in the Third Tidal Cycle by Vortex Tracking Code.

9 and 5 centimeter water depth cases are correct, while all of the secondary vortices for the lower water depth are not identified. This could be attributed to secondary vortices getting damped below the noise level by bottom friction [9, 16] or the code mistakingly joining secondary vortices in close proximity into one object.

To compare secondary structures among the tested water depths, structures corresponding to similar birth times within the tidal cycle are presented. Figure 18 portrays the secondary vortex trajectories of the selected vortices. For all of the tested water depths, the trajectory of the secondary vortex is a function of when it is

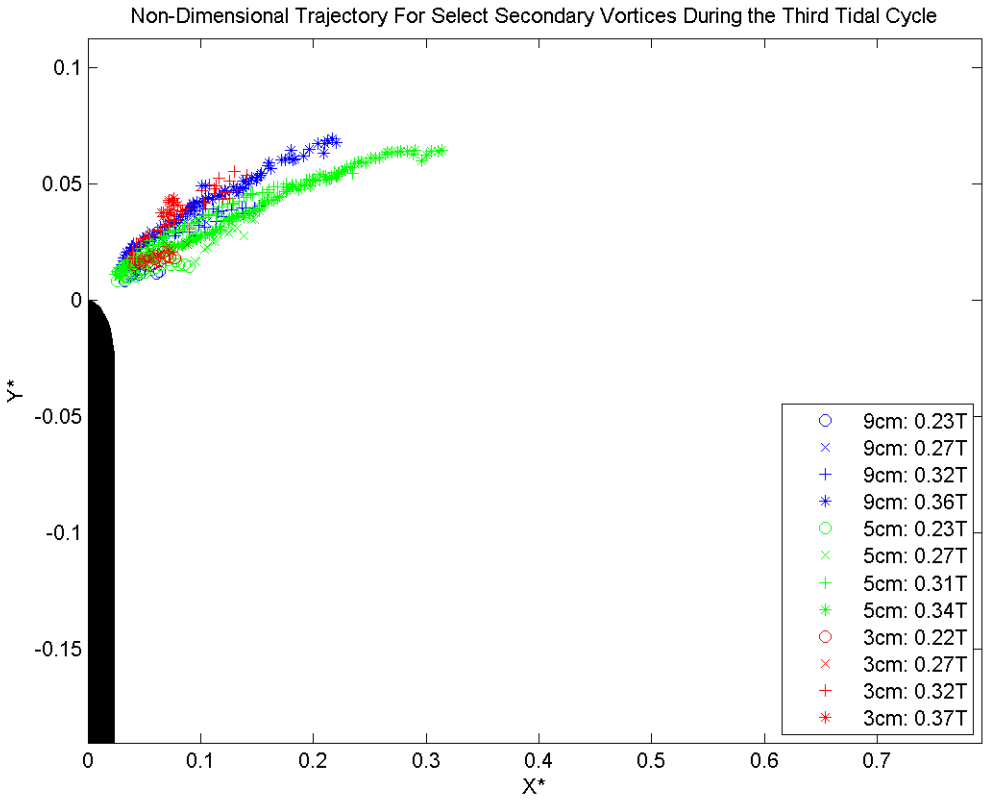

Fig. 18. Non-Dimensional Trajectory of Select Secondary Vortices During the Third Tidal Cycle.

formed during the tidal cycle. A combination of the changing velocities through the channel and the area of recirculation close to the inlet forces the secondary vortices to change trajectory. Those formed later in the cycle travel at higher angles relative to the horizontal axis.

Diameter for the secondary vortices is tracked as a function of the horizontal distance of the centroid. Depicted in Figure 19, the diameter proves to be fairly consistent, however there are fluctuations in the data for the earliest recorded secondary vortex most likely due to inaccurate recognition by the tracking code. After

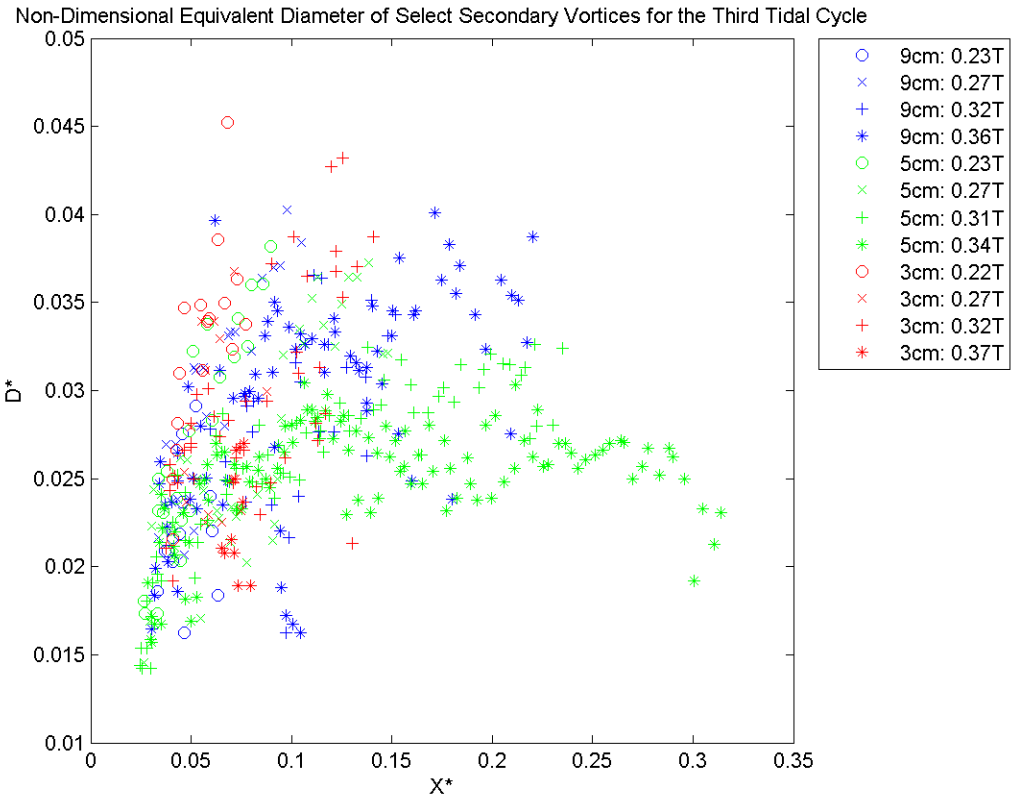

Fig. 19. Non-Dimensional Diameter of Select Secondary Vortices During the Third Tidal Cycle Versus Non-Dimensional Horizontal Location of the Centroid.

the initial generation stage, the secondary vortices seem to reach a steady diameter the further they propagate away from the inlet, which is similar to what is seen with the vortex system for the 5 and 9 centimeter depth cases. Excluding the 3 centimeter depth case, there is at least an order of magnitude difference between the size of the secondary vortices and the final size of the vortex system.

Unlike the diameter calculations, the order of magnitude for the maximum vorticity is similar to that of the vortex system for some of the data points in Figure 20. The erratic behavior is likely caused by the 3D nature of the secondary vortices.

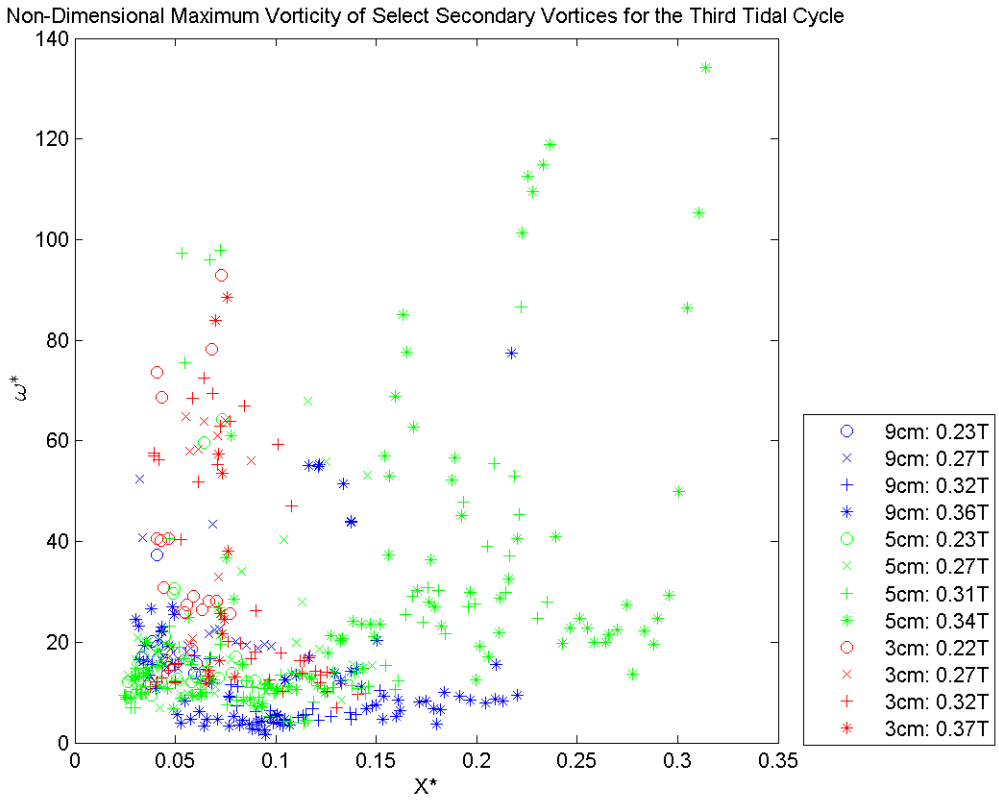

Fig. 20. Non-Dimensional Maximum Vorticity of Select Secondary Vortices During the Third Tidal Cycle Versus Non-Dimensional Horizontal Location of the Centroid.

Contrary to the assumptions in the analysis of the vortex system, the secondary vortex size is on the same order as the water depth, causing more of an influence from bottom friction and 3D effects. The surfacing of these instabilities would cause the fluctuations in the vorticity.

Similar to the trend in the vorticity plot, the circulation, shown in Figure 21, has the majority of its values relatively low. Peaks in the circulation correspond to peaks in the maximum vorticity. This is consistent with expectations since the data for the

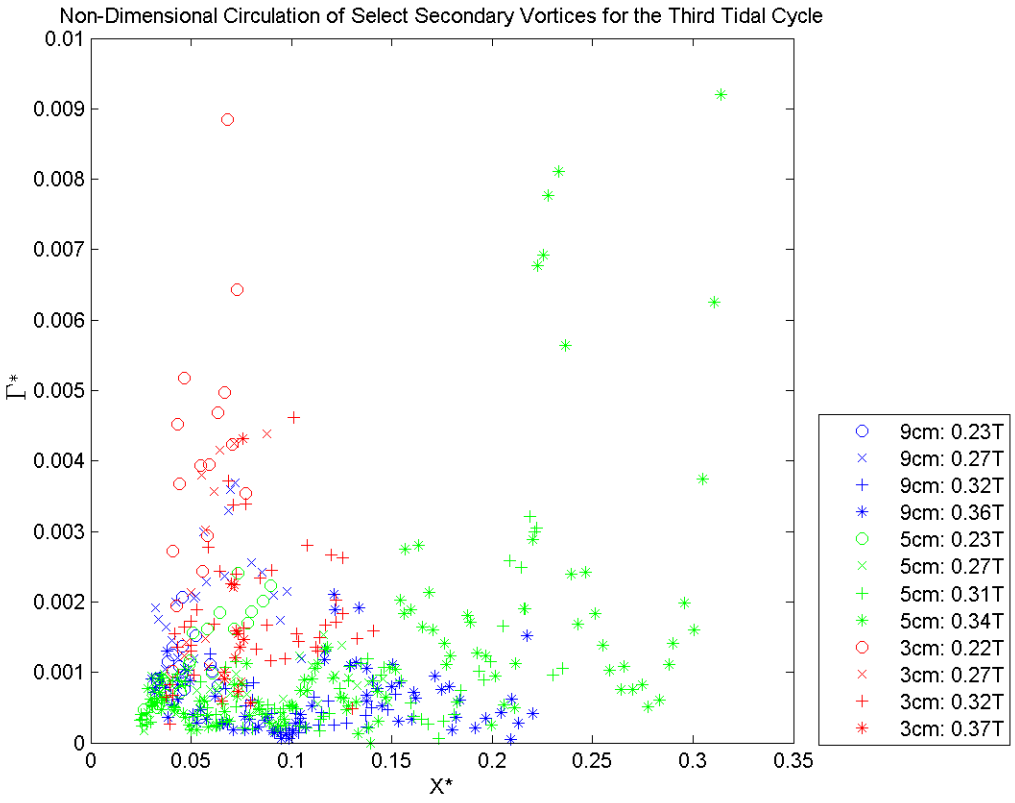

Fig. 21. Non-Dimensional Circulation of Select Secondary Vortices During the Third Tidal Cycle Versus Non-Dimensional Horizontal Location of the Centroid.

diameter is relatively consistent. It is important to note that even with the variations in the data, there is at least one order of magnitude difference between circulation of the secondary vortices and that of the vortex system.

Once the secondary vortices enter the vortex system they are stretched and downwelled. Figure 22 displays an instantaneous swirl strength plot with the corresponding velocity divergence contours. In the divergence plot, there is a large band of downwelling just past the identified vortices in the swirl strength plot. This explains why the satellite vortices lose their shape and become harder to track once they are

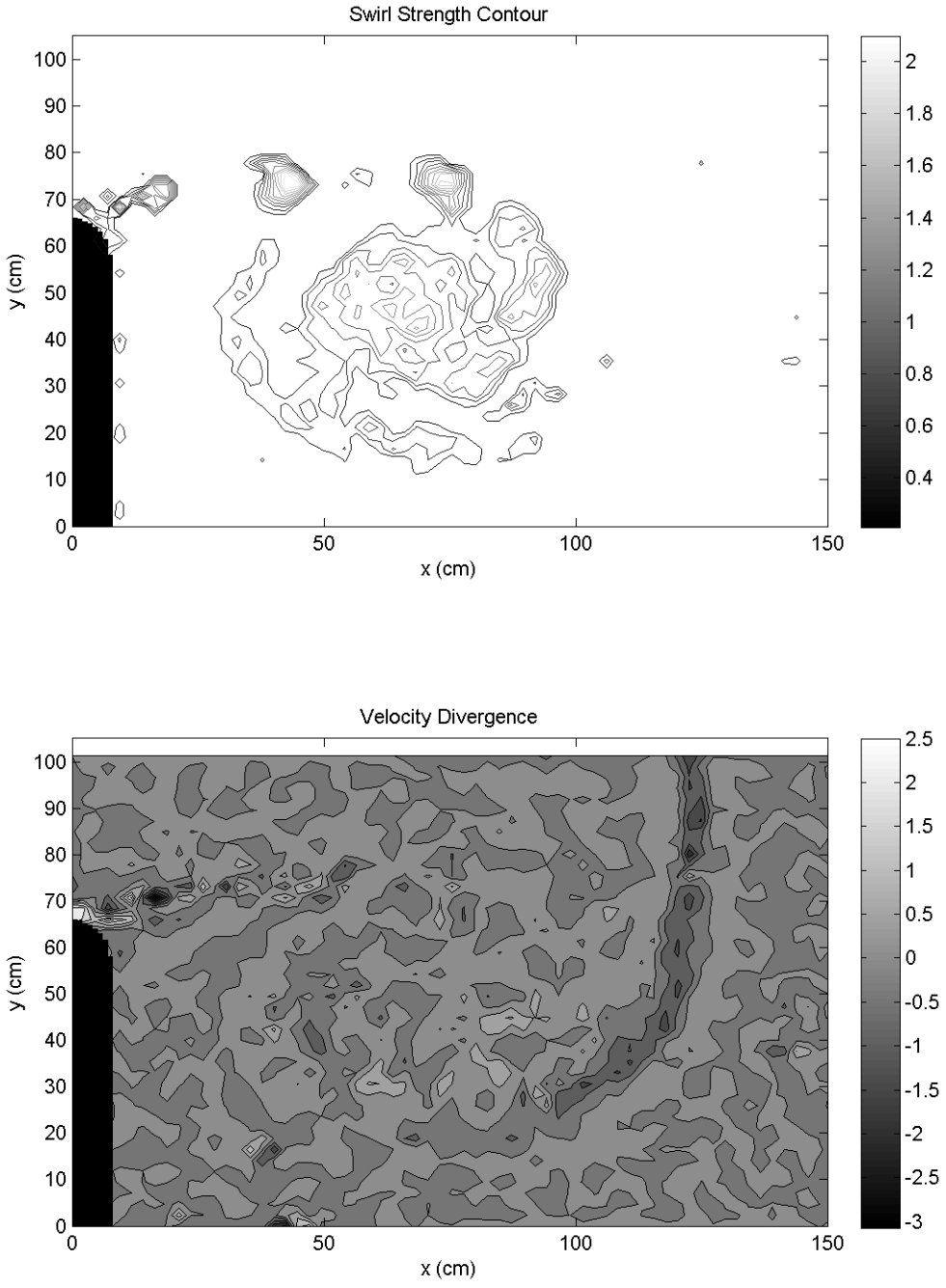

Fig. 22. Instantaneous Swirl Strength and Corresponding Velocity Divergence.

inside the vortex system. As the satellite vortices are downwelled, they are still orbiting the primary vortex. Because the water depths are shallow, the remnants of these rotating structures can still be faintly seen at the surface in the swirl strength calculation. In the swirl strength and object identification movies, this is the area of swirl strength (or identified objects) not part of the vortex system but still orbiting the primary vortex. There is also a band of upwelling and downwelling in the path of the secondary vortices and it works to support the notion of 3D turbulence impacting the vorticity calculations for the secondary vortices and contributing to the errors in the object identification.

CHAPTER VI

CONCLUSION

Laboratory measurements for starting jet vortices formed by tidal flow through an idealized inlet were presented. Raw images were pre-processed to extract surface velocity data from particle image velocimetry. Using the swirl strength, the locations of vortices within the flow field were discovered. With this information, values for trajectory, equivalent diameter, vorticity, and circulation were calculated for the vortex system and secondary vortices and non-dimensionalized using the tidal excursion.

As evidenced by the consistency of data for the vortex system between tidal cycles, the results become repeatable after the second tidal cycle, but because the maximum velocity through the channel was different for each experiment the vortices are not easily compared. However, frictional effects for the 5 and 9 centimeter experiments seemed to be relatively negligible, so comparison between these two experiments relied mainly on differences in maximum velocity through the channel. The results for the non-dimensional trajectory and equivalent diameter of the 5 and 9 centimeter experiments seemed to collapse using the tidal excursion. Since the tidal period was relatively constant, they basically collapsed in non-dimensional space with respect to U_{MAX}. In addition, the maximum velocity through the channel seemed to have an impact on the temporal and spatial peak locations for the vorticity and circulation computations. Peaks occurred faster and closer to the inlet with greater values of maximum velocity.

The properties of the vortices in the 3 centimeter water depth case, however, were heavily impacted by bottom friction. The equivalent diameter was larger than what was expected with respect to the other tested cases and vorticity and circulation peaks were relatively smaller in magnitude. Nevertheless, the temporal and spatial

locations for the vorticity and circulation peaks were consistent with observations from the 5 and 9 centimeter depth experiments. The friction stability analysis proved that the 3 centimeter water depth case would be the one most influenced by friction. Frictional stability occurs at a depth between 5 and 3 centimeters according to the bed friction parameter. The experimental results suggest that friction did not particularly influence the parameters for the 9 and 5 centimeter water depths. So, for a more complete collapse in data between the experiments in non-dimensional space, friction should be included.

The secondary vortices proved to be difficult to track for all of the tested water depths, especially for the 3 centimeter water depth experiment. As a result of incorrect vortex identification and vortex damping, not all of the 3 centimeter water depth case were located. To compare secondary vortices, vortices born the same time within the tidal cycle were analyzed. Like the vortex system variables, the secondary vortices were also non-dimensionalized with the tidal excursion. The non-dimensionalized diameter data seemed to be fairly consistent, but there were fluctuations in the vorticity and circulation computations due to 3D instabilities correlated with the secondary structures.

Based upon the comparison of circulation, the secondary vortices are negligible with respect to the vortex system. However, they may still be instrumental in transport because they do have structure and are able to entrain passive tracers. There are a couple possible solutions for more accurate quantities of the secondary vortices. Either a variable swirl strength threshold would have to be implemented to separate the vortices from the 3D instabilities and accommodate the changing swirl strength of these structures over the course of the tidal cycle, or finer resolution of the PIV data.

REFERENCES

[1] Adrian RJ, Christensen KT, Liu ZC (2000) Analysis and interpretation of instantaneous turbulent velocity fields. Exp Fluids 29:275-290. doi:10.1007/s003489900087

[2] Afanasyev YD (2006) Formation of vortex dipoles. Physics Fluids 18:9. doi:10.1063/1.2182006

[3] Brown CA, Holt SA, Jackson GA, Brooks DA, Holt GJ (2004) Simulating larval supply to estuarine nursery areas: how important are physical processes to the supply of larvae to the Aransas Pass Inlet? Fish Oceanogr 13:181-196. doi:10.1111/j.1365-2419.2004.00285.x

[4] Brown CA, Jackson GA, Brooks DA (2000) Particle transport through a narrow tidal inlet due to tidal forcing and implications for larval transport. J Geophy Res 105(C10):24,141-24,156. doi:10.1029/2000JC000211

[5] Brown CA, Jackson GA, Holt SA, Holt GJ (2005) Spatial and temporal patterns in modeled particle transport to estuarine habitat with comparisons to larval fish settlement patterns. Estuar Coast Shelf Sci 64:33-46. doi:10.1016/j.ecss.2005.02.004

[6] Chen D, Jirka GH (1998) Linear stability analysis of turbulent mixing layers and jets in shallow water layers. J Hydr Res 36(5):815-830.

[7] Grubišić V, Smith RB, Schär C (1995) The effect of bottom friction on shallow-water flow past an isolated obstacle. J Atmos Sci 52:1985-2005. doi:10.1175/1520-0469(1995)052

[8] Jirka GH (2001) Large scale flow structures and mixing processes in shallow flows. J Hydr Res 39(6):567-573.

[9] Kahraman A, Sahin B, Rockwell D (2002) Control of vortex formation from a vertical cylinder in shallow water: effect of localized roughness elements. Exp Fluids 33(1):54-65. doi:10.1007/s00348-002-0467-y

[10] Kashiwai M (1984) Tidal residual circulation produced by a tidal vortex, Part 1: Life-history of a tidal vortex. J Ocea Society of Japan 40:279-294. doi:10.1007/BF02302521

[11] Kashiwai M (1985) TIDICS–Control of tidal residual circulation and tidal exchange in a channel-basin system. J Ocea Society of Japan 41:1-10. doi:10.1007/BF02109926

[12] Kashiwai M (1985) A hydraulic experiment on tidal exchange. J Ocea Society of Japan 41:11-24. doi:10.1007/BF02109927

[13] Kundu PK, Cohen IM (2004) Fluid mechanics, Third edition. Elsevier Academic Press, Amsterdam, The Netherlands, 233 pp

[14] LaVision GmbH (2002) DaVis FlowMaster Software Manual for DaVis 6.2. LaVision GmbH, Göttingen, Germany

[15] National Oceanic and Atmospheric Administration. Transport. Available via http://response.restoration.noaa.gov/book_shelf/934_transport.pdf. Accessed May 2009

[16] Negretti ME, Socolofsky SA, Rummel AC, Jirka GH (2005) Stabilization of cylinder wakes in shallow water flows by means of roughness elements: an experimental study. Exp Fluids 38:403-414. doi:10.1007/s00348-004-0918-8

[17] Nicolau del Roure F (2007) Laboratory studies of eddy structures and exchange processes through tidal inlets. M.S. thesis, Department of Civil Engineering, Texas A&M University, USA

[18] Nicolau del Roure F, Socolofsky SA, Chang KA (2009) Structure and evolution of tidal starting-jet vortices at idealized barotropic inlets. J Geophy Res: Oceans 114:C05024. doi:10.1029/2008JC004997

[19] Raffel M, Willert C, Kompenhan J (1998) Particle image velocimetry: a practical guide. Springer-Verlag, Berlin, Germany, 159 pp

[20] Signell RP, Geyer WR (1991) Transient eddy formation around headlands. J Geophy Res: Oceans 96(C2):2561-2575. doi:10.1029/90JC02029

[21] Socolofsky SA, Jirka GH (2004) Large scale flow structures and stability in shallow flows. J Envirn Engrg Sci 3(5):451-462. doi:10.1139/s04-032

[22] Wells MG, van Heijst GF (2003) A model of tidal flushing of an estuary by dipole formation. Dynamics of Atm and Oceans 37:223-244. doi:10.1016/j.dynatmoce.2003.08.002

APPENDIX A

SUMMER 2008 EXPERIMENTS

Anticipating the satellite vortices would impact the dipole system, a series of dye visualizations were conducted using localized enhanced bottom roughness to damp the smaller structures.

A. Introduction

Effects of bottom friction have been examined numerically and experimentally for environmental flows. For atmospheric vortex generation behind an obstacle, Grubišić et al. used a numerical model to simulate stabilized wake formation as a result of bottom friction in addition to analyzing the ability of bottom friction to create and attenuate vorticity. Through their studies, they confirmed that bottom friction creates vorticity when there are large fluctuations in depth or roughness and increasing the friction parameter stabilizes the wake formation. However, for their application, the vorticity creation was dominated by hydraulic jumps rather than bottom friction. They do note that vorticity generation in oceanic flows is primarily due to bottom friction [7].

Most recently, laboratory studies have been conducted on wake stabilization behind a cylinder due to localized bottom roughness elements. Similar to Grubišić et al., data presented by Kahraman et al. and Negretti et al. conclude that wakes can be stabilized due to enhanced bottom friction. By examining horizontal sections of the flow, Kahraman et al. determined that increased roughness not only weakens formation at the bed but also mid-depth [9]. Although Kahraman et al. varied the friction factor, Negretti et al. determined an estimate for the size of the roughness

element as a function of the boundary layer thickness and the obstacle diameter [16]. Both experimental studies indicate the localized roughness elements have a global effect on the flow since the upstream and downstream conditions are affected.

Using the localized enhanced bottom roughness approach, laboratory experiments for this study were designed to damp secondary vortices in tidal flow through an idealized inlet. Unlike the previous laboratory studies, the aim is to attenuate a secondary part of the flow. Although the roughness elements are expected to perform similar to the previous work, the influence on the overall flow and dipole structure are unknown. This study is the first step in providing proof of concept for utilizing localized roughness elements for impeding secondary structures in a tidal inlet application.

B. Experimental Setup

Once again, experiments were conducted in the 15.0 by 5.5 meter shallow water basin at the Institute for Hydromechanics at the University of Karlsruhe, Germany. The same layout and fluid conditions described in Chapter II were implemented for this round of experiments to provide consistency. For this study, the water depth was not varied and was held constant at 5 centimeters for 4 consecutive tidal cycles. Similar to Kahraman et al. and Negretti et al., a bottom roughness element was added to the layout to damp the smaller structures formed once the starting-jet dipole propagates away from the inlet boundary. Placement of the grid was based on the known trajectory of the dipole. As evidenced in Figure 9, during the tidal cycle the dipole tends to move laterally away from the center of the inlet and migrate back toward the center as the tide reverses. The mesh grid was designed to fit within this space. Figure 23 illustrates the setup with the addition of a 0.59 by 0.44 meter

bottom roughness element placed 0.40 meters away from the center of the inlet.

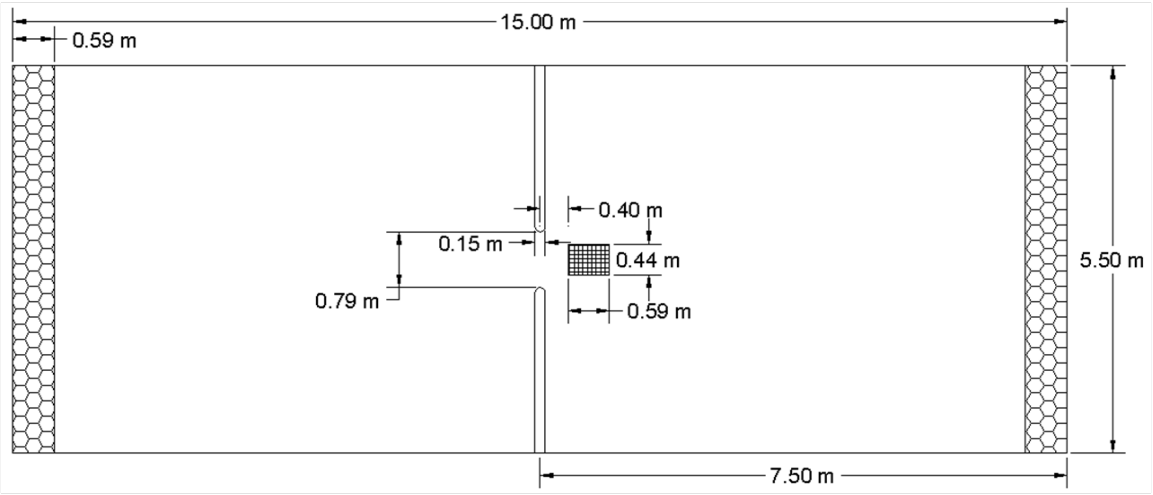

Fig. 23. Shallow Water Wave Basin Including Idealized Inlet Configuration and Roughness Element.

The mesh grid was constructed of interwoven 1 millimeter diameter steel wire creating a 6 by 6 millimeter opening between wires [16]. Dye was dispensed on either side of the inlet mouth within the small boundary layer to illuminate the dipole formation. Due to camera limitations, a video camera was mounted on a bridge straddling the basin looking downstream. The camera field of view is shown in Figure 24 as a dipole moves over the roughness element during the second tidal cycle. Tests were run with and without using the roughness element.

C. Results and Discussion

Full versions of the experiments are included in the electronic supplement described in Appendix B. Not surprising, the tests conducted without the bottom roughness

Fig. 24. Dipole Propagating Past Enhanced Bottom Roughness Element.

element behave in the same manner as the other experiments described in this thesis. Vortices of opposite rotation form on either side of the inlet mouth, and once the dipole propagates away from the inlet boundary, a number of secondary structures are created as a result of continuous flow moving past the inlet edge. On the reverse tide, the dipole propagates straight away from the inlet; except for the first tidal cycle when it stalls directly in front of the inlet mouth and propels forward at the beginning of the next cycle. After multiple cycles, there is vortex interaction at the end of the basin but it does not interfere with the flow near the inlet opening.

With the experiments implementing the bottom roughness element, the vortices which compose the dipole are formed, and once they propagate away from the inlet boundary the roughness element appears to damp the secondary structures. Because

the grid extends across the middle of the opening, the flow must overcome more friction and the dipole does not move as far downstream as the case without the localized roughness patch. As a result, the dipole is drawn slightly back toward the inlet, creating a stationary vortex; and is partially damped due to its interaction with the roughness element. When the next cycle begins, new vortices form at the mouth of the inlet and the dipole from the previous cycle is pushed away from the inlet with a skewed trajectory. The skewed trajectory is likely due to uneven dampening of the dipole during the encounter with the roughness element on the reverse tide. Unlike the base experiment, vortex interaction occurs before the end of the basin due to the relatively slower propagation velocities.

D. Conclusion

Applying the localized roughness grid across the center of the inlet effected the horizontal movement of the dipole, but it showed promise for dissipating the secondary vortices in this flow field. The size of the bottom roughness element is critical for attenuating the secondary structures and could actually work to enhance instabilities if incorrect dimensions are used [16]. PIV measurements would confirm if residual disturbances occur.

Placement of the grid might also present a dilemma. The current location only damps select secondary structures. As the primary vortices detach from the inlet boundary, some secondary vortices are still being absorbed into the vortex system. If roughness strips were used instead of extending the grid across the center of the inlet, the dipole should travel the same distance as those created in the non-grid experiments. Because the secondary vortices change trajectory depending on their birth in the tidal cycle, as depicted in Figure 18, the width of these strips could still influence

the center flow thus influencing the dipole trajectory. Previous measurements, at the bed and mid-plane, confirm that even small amounts of roughness weaken the formation of vortex structures [9]. That being said, this act may instill 3D instabilities on an otherwise predominately 2D structure.

APPENDIX B

ELECTRONIC SUPPLEMENT

The DVD supplement includes folders which contain the following:

- Movies: Visualizations of calculated velocity, swirl strength, and vortex identification for each experiment presented in the thesis are included. For the velocity vector field movies, every other velocity vector is represented and is shown with the corresponding swirl strength. The object identification movies, also displayed with the corresponding swirl strength, use a magenta "x" to indicate the location of peak swirl strength and a black "x" represents the calculated centroid for each object. All movies are real-time and begin with the second tidal cycle.

- Dye Studies: Dye studies illustrating the preliminary setup for enhanced bottom roughness to damp secondary vortices are presented.

VITA

Kerri Ann Whilden received her Bachelor of Science degree in civil engineering from Lehigh University located in Bethlehem, Pennsylvania in May 2007. While in school, she worked part–time for a civil engineering firm doing site development and traffic engineering. She continued to work at this company until she left to pursue a Master of Science degree in ocean engineering at Texas A&M University in August 2007. In May 2008, she wrote a conference paper entitled "Laboratory Measurements of Shallow Starting–Jet Vortices Formed by Tidal Flow through an Idealized Inlet" for the Inaugural International Conference of the Engineering Mechanics Institute held at the University of Minnesota, and presented updated results at the EuroMech Colloquium in Ancona, Italy in June that same year. After spending the summer of 2008 conducting experiments at the Institute for Hydromechanics at the University of Karlsruhe, Germany, she presented another conference paper entitled "Formation and Evolution of Tidal Jet Vortices through an Idealized Inlet" for the International Symposium on Shallow Flows at Hong Kong Institute of Science & Technology in December 2008. After receiving her Master of Science degree in August 2009, she plans to continue her studies at Texas A&M University in the Ph.D. program focusing on laboratory and field measurements of tidal flows.

Kerri Ann Whilden can be reached at Coastal & Ocean Engineering Division, Zachry Department of Civil Engineering, Texas A&M University, MS 3136, College Station, TX 77843, or through email at kerriwhilden@gmail.com.